Energy & Environmental Science

ROYAL SOCIETY OF CHEMISTRY

REVIEW

View Article Online
View Journal | View Issue

Cite this: *Energy Environ. Sci.*, 2022, **15**, 3750

Recent advances and perspectives in aqueous potassium-ion batteries

Xiao Zhang,†[ab] Ting Xiong,†[b] Bing He,[b] Shihao Feng,[a] Xuanpeng Wang,*[c] Lei Wei*[b] and Liqiang Mai*[a]

Received 16th May 2022,
Accepted 26th July 2022

DOI: 10.1039/d2ee01573k

rsc.li/ees

Aqueous potassium-ion batteries (AKIBs), utilizing fast diffusion kinetics of K^+ and abundant electrode resources, are an emerging technology offering high power density and low cost. Many efforts have been made by far to enhance the electrochemical performances of AKIBs, and some encouraging milestones have been achieved. To provide a deep understanding of the progress, challenges, and opportunities of the emerging AKIBs, the recent advances in both cathode and anode materials, and electrolytes of the AKIB systems are comprehensively summarized and discussed. Additionally, the research efforts on the optimization of electrode material properties, the revealing of the reaction mechanism, the design of electrolytes, and the full cell fabrication for AKIBs are highlighted. Finally, insights into opportunities and future directions for achieving high-performance AKIBs and their applications are proposed.

Broader context

Compared with traditional Li-ion batteries with toxic and flammable organic-based electrolytes, aqueous potassium-ion batteries (AKIBs) with mild electrolytes have shown great advantages in large-scale energy storage systems and wearable devices due to their good safety, low cost, and environmental friendliness. Despite recent breakthroughs in cathodes, anodes, and electrolytes, AKIBs still face significant challenges in energy density and cycle life, including narrow voltage windows, electrode dissolution, corrosion, and unexpected by-products. These fundamental problems may lead to irreversible capacity loss, poor cycling stability, and short circuit, severely limiting the efficient storage of K^+ ions and the future applications of AKIBs. Here, a comprehensive and critical review on the recent advances on AKIBs is provided. The recent research efforts on the innovative electrode and electrolyte designs, the revealing of the reaction mechanism, and the full cell fabrication for AKIBs are highlighted. Based on the current developments, future research directions and perspectives toward high-performance AKIBs and their applications are proposed, guiding the development of this highly exciting field.

1. Introduction

The depletion of fossil fuels, along with the severe environmental pollution, motivates us to explore renewable energy sources. While most renewable energy sources are intermittent, it is required to develop large-scale stationary energy storage systems (ESSs) to utilize them efficiently.[1,2] Among various ESSs, the rechargeable battery technologies act as the primary energy storage solution due to their flexibility, low geographic requirements, and high energy conversion efficiency.[3] Lithium-ion batteries (LIBs) have dominated the field for electric vehicles and portable electronic devices, while battery fire accidents occur frequently, mainly caused by the volatile and flammable organic electrolyte, which significantly increase the safety risks of LIBs.[4–7]

Besides organic electrolytes, aqueous electrolytes could also be applied in batteries. Rechargeable LIBs based on aqueous electrolytes were firstly proposed in 1994 by Dahn *et al.*[8] Since then, extensive research has been made toward developing various aqueous rechargeable metal-ion batteries, including non-Li^+ (such as Na^+, K^+, Zn^{2+}, Mg^{2+}, Ca^{2+}, Al^{3+}, *etc.*) batteries.[9–21] Aqueous batteries are particularly promising for solving current issues faced by the commercial LIBs, thanks to the following outstanding properties: (1) the safety of batteries is greatly improved by using aqueous electrolytes; (2) the cost of aqueous batteries is expected to be largely reduced due to the absence of strict assembly conditions and expensive organic solvents; and (3) the electrical conductivity of aqueous

[a] *State Key Laboratory of Advanced Technology for Materials Synthesis and Processing, Wuhan University of Technology, Wuhan 430070, P. R. China. E-mail: mlq518@whut.edu.cn*
[b] *School of Electrical and Electronic Engineering, Nanyang Technological University, Singapore 639798, Singapore. E-mail: wei.lei@ntu.edu.sg*
[c] *Department of Physical Science & Technology, School of Science, Wuhan University of Technology, Wuhan 430070, P. R. China. E-mail: wxp122525691@whut.edu.cn*
† X. Z. and T. X. contributed equally to this work.

electrolytes is two orders of magnitude higher than that of organic electrolytes.

In this new family of aqueous rechargeable batteries, aqueous potassium-ion batteries (AKIBs) are garnering significant attention. AKIBs are rocking chair batteries similar to the traditional LIBs. The schematic configuration of a typical AKIB is shown in Fig. 1a, including a cathode (Prussian blue analog (PBA)), an anode ($KTi_2(PO_4)_3$), and an aqueous electrolyte. During the charging process, K^+ ions, as charge carriers, are released from the cathode material, then travel across the electrolyte, and are eventually inserted into the anode material, while electrons also transfer to the anode through the external circuit. While for the discharging process, the intercalated K^+ ions are extracted from the anode and then re-intercalated into the cathode. At the same time, the electrons in the external circuit move from the anode to the cathode. It is well known that the AKIBs show the following advantages: (1) K shows a relatively low redox potential (−2.9 V *vs.* the standard hydrogen electrode (SHE)), leading to a high potential energy density; (2) K is 1000 times more abundant than Li in the Earth's crust, promising in lowing the battery cost; (3) low Lewis acidity of K^+ results in the smallest hydrated ionic size (3.31 Å) in an aqueous solvent, which facilitates its fast diffusion (Fig. 1b and c).[22] Therefore, AKIBs are considered one of the ideal electrochemical devices for large-scale ESSs. However, like many other aqueous batteries, AKIBs are hampered by two prevalent issues, namely limited energy density and suboptimal lifetime. Fundamentally, the inherent hydrogen evolution reaction (HER) and oxygen evolution reaction (OER) of water enable AKIBs with a narrow electrochemical stable window (ESW) of 1.23 V, leading to insufficient energy density (Fig. 1d).[23–26] In addition, side reactions occur between the electrode materials and H_2O or precipitated O_2 during the discharging/charging processes, which cause structural degeneration of the electrode material, thus affecting the cycle stability of the battery. Moreover, the dissolution of active electrode materials occurs in aqueous electrolytes due to the high dielectric property of water.

Pioneering work on the electrochemical behavior of Prussian blue (PB) for K^+ storage was first performed by Neff *et al.* in 1978.[10] Since then, researchers have made remarkable achievements in AKIBs *via* materials design and electrolyte optimization (see Fig. 1e). However, to date, a systematic summary on the latest development of AKIBs is still lacking. This review focuses on the latest advances and perspectives in electrode materials (cathodes and anodes) and electrolytes of AKIBs, then discusses current progress on the optimization of electrode material properties, the understanding of the reaction mechanism, the design of electrolytes, and the full cell fabrication. Finally,

Xuanpeng Wang

Xuanpeng Wang is an Assistant Professor at the School of Science, Wuhan University of Technology (WUT). He received his PhD degree from WUT in 2019. His current research focuses on material synthesis, device design, in situ characterization of new-type potassium-ion batteries and sodium-ion batteries.

Lei Wei

Lei Wei is an Associate Professor at Nanyang Technological University in Singapore. He received the BE degree from the Wuhan University of Technology in 2005 and the PhD degree from the Technical University of Denmark in 2011. Then he joined the Massachusetts Institute of Technology as a postdoctoral associate. In 2014, he joined the Nanyang Technological University in Singapore as a Nanyang Assistant Professor. In 2019, he was promoted to Associate Professor with tenure. His main research interests are fiber-based devices, multi-functional fibers and fabrics, bio-fiber interfaces, and in-fiber energy generation and storage. He currently serves as the Director of Centre for Optical Fibre Technology (COFT) at Nanyang Technological University. He also serves as the chairman of the IEEE Photonics Society Singapore Chapter and the chair of Optica (formerly OSA) Singapore Section.

Liqiang Mai

Liqiang Mai is a Chair Professor of Materials Science and Engineering at the Wuhan University of Technology (WUT), Dean of the School of Materials Science and Engineering at WUT, and Fellow of the Royal Society of Chemistry. He received his PhD degree from WUT in 2004 and carried out his postdoctoral research at Georgia Institute of Technology in 2006–2007. He worked as an advanced research scholar at Harvard University in 2008–2011 and the University of California, Berkeley in 2017. His current research interests are focused on new nanomaterials for electrochemical energy storage and micro/nano energy devices.

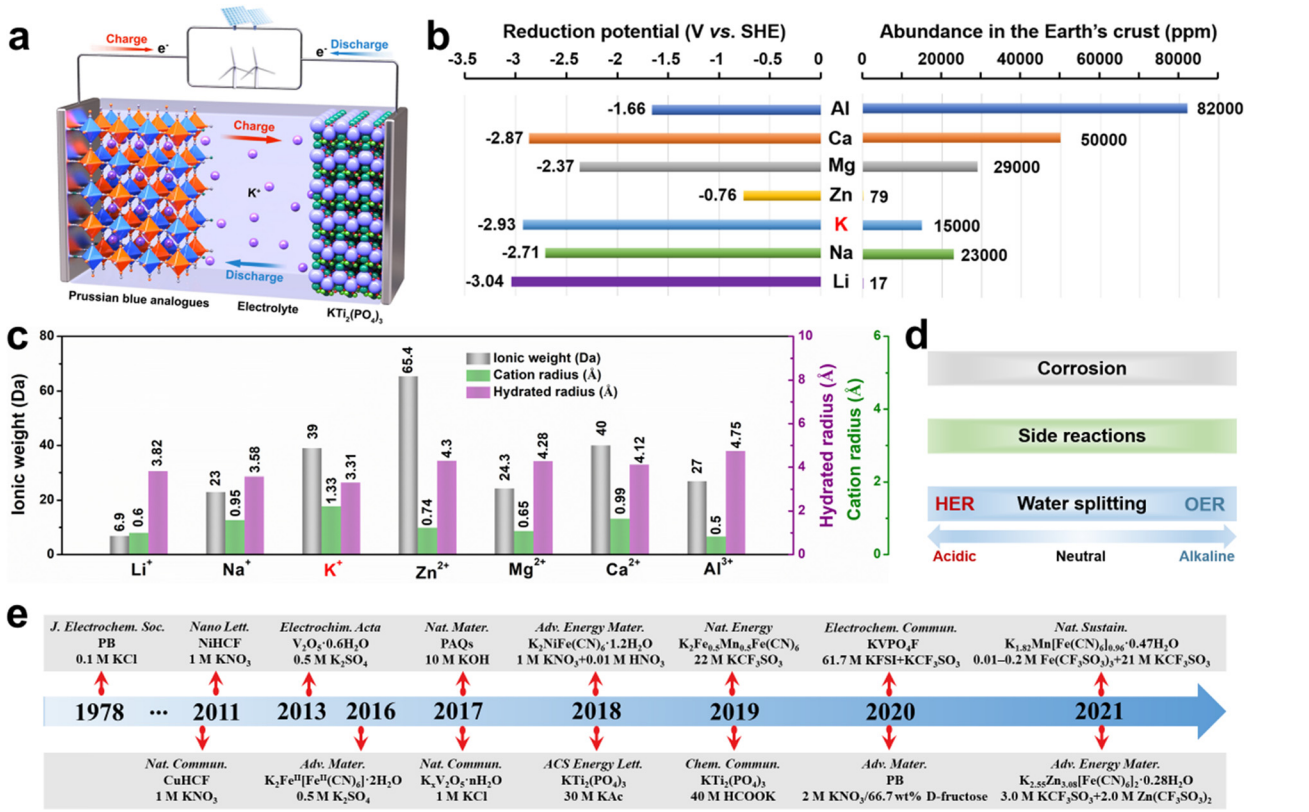

Fig. 1 (a) Schematic illustration of AKIB. (b) Comparison of reduction potential and abundance in the earth of different metals. (c) Comparison of hydrated radius, cation radius, and ionic weight of metal-ion charge carriers. (d) The major challenges to be addressed in AKIBs. (e) Brief development history of the representative advancement in aqueous K^+ storage.

insights into the existing challenges and future development direction of high-performance AKIBs are summarized.

2. Electrodes for AKIBs

For the electrode materials for AKIBs, their redox potentials should be in or near the electrolysis potential range of water. The red dotted lines represent the electrolytic potentials of H_2 and O_2 generated under neutral pH conditions (Fig. 2). Electrode materials within this range can work normally, otherwise the electrode will continue to electrolyze water. A summary of the representative anode and cathode materials with redox potentials for AKIBs is given. As revealed, PB, PBAs, NASICON-type $Na_3V_2(PO_4)_3$, and MXenes exhibit desired potentials as cathodes for AKIBs. Some vanadium-based oxide materials offer desired potentials as both cathode and anode. $KTi_2(PO_4)_3$ with low potential is the most widely-adopted anode for AKIBs. Organic materials and alloys can provide low redox potentials, while metal oxides and sulfides exhibit relatively high redox

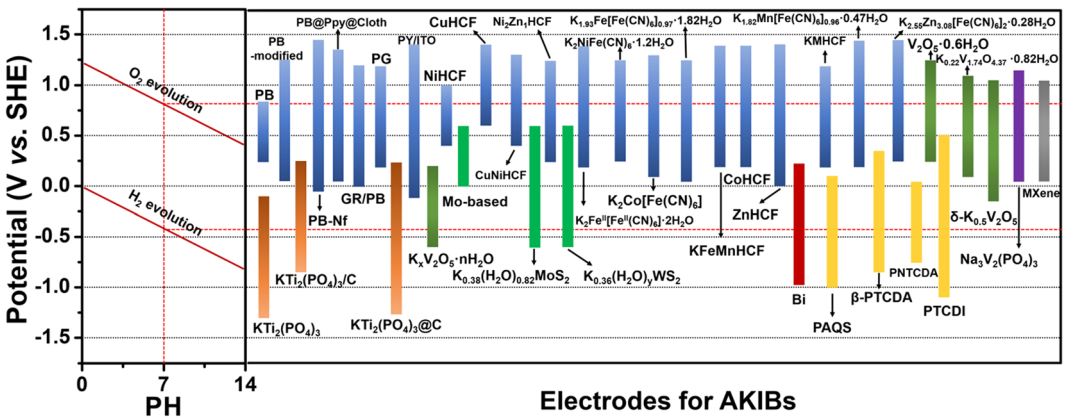

Fig. 2 Electrochemical stability windows of aqueous electrolytes and redox potentials of various electrode materials for AKIBs.

potentials. Therefore, in order to pursue state-of-the-art AKIBs, it is imperative to discover novel cathode materials with high redox potential and high-capacity anode materials, both of which could show stable electrochemical stability.

2.1. Cathode materials

Similar to LIBs, the energy/power density and cost of AKIBs are dependent on the cathode material.[27,28] Thus, developing and designing cathode materials with high discharge potential, high specific capacity, and robust crystal structure that allow intercalation and deintercalation of K^+ is the major challenge for AKIBs. To date, materials that have been demonstrated as viable K^+ host materials are limited, including PB, PBAs, vanadium-based materials, $Na_3V_2(PO_4)_3$, and MXenes. The cathode materials and corresponding electrochemical performances are summarized (Table 1). Furthermore, the K^+ storage behavior, electrochemical performance, mechanisms, current issues, and optimization strategies of these cathode materials are discussed in this section.

2.1.1. PB and PBAs. PB and PBAs have received extensive attention due to their open framework, diverse structures, simple preparation, and low cost.[56,57] The general formula of PBAs is defined as $A_xPR(CN)_6(H_2O)_n$ ($0 < x < 2$), where *A* is the alkali-metal ion (K, Na, or Li) and P (or R) is the transition-metal ion (Co, Fe, Ni, and Mn).[58–61] The cubic framework endows PBAs with large void sites for the rapid storage of alkali metal ions in aqueous electrolytes. However, the relative amounts of A, P, $R(CN)_6$ and structural moisture content may not be uniform due to defects in the framework.

The crystal structure of PB is a rigid cubic framework ($a = b = c = 10.13$ Å) with Fe^{III} and Fe^{II} alternately occupying hexahedral vertex positions linked by C≡N ligands, which can accommodate more K^+ insertion/extraction (Fig. 3a). The electrochemical redox behavior of PB thin films in KCl-based electrolytes was investigated as early as 1978 by Neff *et al.*[10] The electrode was bright blue when the scanning potential was 0.6 V *vs.* saturated calomel electrode (SCE), and then became colorless at 0.0 V *vs.* SCE. The color change of the electrode was caused by the reaction between PB and ''Everitt's salt''. Subsequently, Itaya *et al.* discovered that the electrochemical behavior of PB-modified electrodes was related to the current density used to prepare PB films.[33] The films prepared at higher current densities may contain incompatible $Fe(CN)_6^{4-}/Fe(CN)_6^{3-}$ and Fe^{2+}/Fe^{3+} ions, which showed sharp current peaks in the cyclic voltammetry (CV) curves. Higher charge loss indicated the existence of many non-coordinating ions in the films prepared at higher current densities. Honda *et al.* prepared a thin PB layer on Nafion (Nf) substrate by a surface complexation method.[34] The composite electrode exhibited good electrochemical stability and a stable voltage of 0.68 V in the self-discharge test. They found that the battery discharge rate was significantly dependent on the amount of iron remaining in the Nf film. The iron ions in the matrix could act as electronic mediators between the PB electrodes and the surface of the matrix. Zarbin *et al.* developed a wet chemical method to prepare graphene (GR)/PB nanocomposites as cathode for AKIBs.[30] Compared with pure PB film, the CV curves of GR/PB film exhibited sharper peaks, which benefited from the fast electron transfer provided by graphene in the film. Recently, commercially available PB as AKIB cathode was investigated in KNO_3-based electrolyte by Shu's group.[29] Based on the redox of Fe^{2+}/Fe^{3+}–N couple (0.2–0.4 V *vs.* Ag/AgCl), the PB cathode achieved a stable and high capacity of 84.7 mA h g^{-1} at 1C (Fig. 3b and c). Also, benefiting from the robust metal–organic framework, this cathode exhibited a stable cycle performance with 500 cycles for K^+ storage (Fig. 3d). The slight shift (about 0.1°) of the *ex situ* XRD pattern indicated the subtle lattice shrinkage and expansion caused by the K^+ intercalation and deintercalation of PB (Fig. 3e).

Compared with PB, PBAs are more favored due to their diverse structures and excellent electrochemical performance. Recently, Cui *et al.* reported a series of PBAs, which showed excellent K^+ storage behavior in AKIBs. Initially, nickel hexacyanoferrate (NiHCF) was synthesized using a precipitation method and then investigated for K^+ storage.[36,62] The structure of NiHCF is similar to that of PB, and Ni^{2+} occupies nitrogen coordination, replacing Fe^{3+} in PB (Fig. 4a). It was found that NiHCF reacted with K^+ at 0.69 V *vs.* SHE in KNO_3-based electrolyte (Fig. 4b). NiHCF possessed a discharge capacity of 59 mA h g^{-1} at C/6. Moreover, the excellent rate capability (with 66% capacity retention at 41.7C) and superior stability (93% capacity retention after 5000 cycles) were delivered. Subsequently, they synthesized copper hexacyanoferrate (CuHCF) using a similar method.[35,62] The co-precipitation process of CuHCF was slower than that of PB. Due to the existence of excess Cu^{2+}, highly crystalline and polydisperse nanoparticles could be grown in an orderly manner. The structure of CuHCF is also similar to that of PB, with Cu(II) occupying the nitrogen-coordinated P site and Fe(III) occupying the carbon-coordinated R site (Fig. 4c). CuHCF electrode realized a discharge potential of 0.946 V *vs.* SHE in KNO_3-based electrolyte, which exceeded that of the NiHCF electrode (0.69 V) (Fig. 4d). A similar specific capacity of 59.14 mA h g^{-1} was recorded, indicating that high energy density could realize in the CuHCF electrode for AKIBs. In addition, the CuHCF electrode delivered higher rate capability (67% capacity retention of its initial capacity at 83C) and longer lifetime (17% capacity loss after 40 000 cycles) compared to the NiHCF electrode. Additionally, hexacyanoferrate (ZnHCF) was utilized as cathode materials in Na_2SO_4, K_2SO_4, and $ZnSO_4$ solutions.[40] ZnHCF exhibits a rhombic structure, which is different from the cubic structure. FeC_6 octahedra and ZnN_4 tetrahedra are collected by C≡N ligands to generate a 3D open framework (Fig. 4e). In the K_2SO_4 electrolyte, a pair of redox peaks at 0.83/1.03 V *vs.* Ag/AgCl appeared higher than those of $ZnSO_4$ and Na_2SO_4 electrolytes (Fig. 4f). The specific capacity of ZnHCF in K_2SO_4 electrolyte at 5C was 69.7 mA h g^{-1}, which exceeded that of $ZnSO_4$ electrolyte (64.4 mA h g^{-1}), but lower than that of Na_2SO_4 electrolyte (71.4 mA h g^{-1}).

Although the above-developed PBA-based AKIBs have shown satisfactory performance, their low K^+ containing amount limits the reversible capacity. In this regard, Wang *et al.* reported K-rich iron hexacyanoferrate ($K_2Fe^{II}Fe^{II}(CN)_6{\cdot}2H_2O$)

Table 1 Summary of cathode materials and the corresponding electrochemical performance of AKIBs

Cathode materials	Electrolyte	Working potential range	Specific capacity/current	Capacity retention/cycles/current	Rate capability/current	Ref.
$Fe_4^{III}[Fe^{II}(CN)_6]_3$ $3.4H_2O$	3.75 M KNO_3	−0.25 to 0.85 V *vs.* Ag/AgCl	84.7 mA h g^{-1}/1C	80.8%/1000/10C	68.5 mA h g^{-1}/6C	29
GR/PB	0.1 M KCl	−0.2 to 1.0 V *vs.* Ag/AgCl	141.2 mA h g^{-1}/93 mA g^{-1}	—	∼40 mA h g^{-1}/2.3 A g^{-1}	30
PB-K//AC	1 M KNO_3 + 60.0 wt% maltose	0–2 V *vs.* AC	69.6 mA h g^{-1}/0.5 A g^{-1}	66.7%/2000/2 A g^{-1}	—	31
PB@PPy@Cloth	1 M KCl	−0.2 to 1.1 V *vs.* SCE	125 mA h g^{-1}/100 mA g^{-1}	89.5%/500/500 mA g^{-1}	52 mA h g^{-1}/2000 mA g^{-1}	32
PB	0.1 M KCl	0–0.6 V *vs.* SCE	—	—	—	10
PB-modified Pt electrode	1 M KCl	−0.2 to 1.0 V *vs.* SCE	—	—	—	33
PB-Nf film	1 M KCl	−0.3 to 1.2 V *vs.* SCE	—	—	—	34
CuHCF	1 M KNO_3 + 0.01 M HNO_3	0.6–1.4 V *vs.* SHE	59.1 mA h g^{-1}/0.83C	83%/40 000/17C	40.1 mA h g^{-1}/83C	35
NiHCF	1 M KNO_3 + 0.01 M HNO_3	0.4–1.0 V *vs.* SHE	59 mA h g^{-1}/10 mA g^{-1}	∼93%/5000/498 mA g^{-1}	38.9 mA h g^{-1}/2502 mA g^{-1}	36
CuNiHCF	1 M KNO_3	0.4–1.3 V *vs.* SHE	65 mA h g^{-1}/50 mA g^{-1}	91%/2000/500 mA g^{-1}	—	37
$K_2Co[Fe(CN)_6]$	0.5 M K_2SO_4	0–1.2 V *vs.* Hg/HgO	112 mA h g^{-1}/400 mA g^{-1}	95%/1000/4000 mA g^{-1}	80 mA h g^{-1}/4000 mA g^{-1}	38
$K_2Fe^{II}[Fe^{II}(CN)_6]\cdot 2H_2O$	0.5 M K_2SO_4	0–1.2 V *vs.* Ag/AgCl	120 mA h g^{-1}/200 mA g^{-1}	96%/500/500 mA g^{-1}	93 mA h g^{-1}/3000 mA g^{-1}	39
ZnHCF	0.5 M K_2SO_4	−0.2 to 1.2 V *vs.* Ag/AgCl	69.7 mA h g^{-1}/300 mA g^{-1}	—	—	40
Ni_2Zn_1HCF	0.6 M K_2SO_4	0–1 V *vs.* SCE	66.0 mA h g^{-1}/300 mA g^{-1}	89.6%/30 000/30 A g^{-1}	43.8 mA h g^{-1}/60 A g^{-1}	41
$K_{1.93}Fe[Fe(CN)_6]_{0.97}\cdot 1.82H_2O$	1 M KNO_3	−0.2 to 1.0 V *vs.* SCE	142 mA h g^{-1}/75 mA g^{-1}	88%/300/1500 mA g^{-1}	40 mA h g^{-1}/9000 mA g^{-1}	42
$K_2NiFe(CN)_6\cdot 1.2H_2O$	1 M KNO_3 + 0.01 M HNO_3	0–1 V *vs.* SCE	77.4 mA h g^{-1}/400 mA g^{-1}	98.6%/5000/2400 mA g^{-1}	42.1 mA h g^{-1}/40 A g^{-1}	43
KFeMnHCF	22 M KCF_3SO_3	0–1.2 V *vs.* Ag/AgCl	135 mA h g^{-1}/65 mA g^{-1}	90%/10 000/13 A g^{-1}	85 mA h g^{-1}/15.6 A g^{-1}	44
CoHCF	22 M KCF_3SO_3	0–1.2 V *vs.* Ag/AgCl	90.4 mA h g^{-1}/20 mA g^{-1}	70.0%/1000/600 mA g^{-1}	65.6 mA h g^{-1}/100 mA g^{-1}	45
$K_{1.82}Mn[Fe(CN)_6]_{0.96}\cdot 0.47H_2O$	21 M KCF_3SO_3 + 0.01–0.2 M $Fe(CF_3SO_3)_3$	0–1.25 V *vs.* Ag/AgCl	160 mA h g^{-1}/300 mA g^{-1}	∼100%/13 0000/2500 mA g^{-1}	95 mA h g^{-1}/7000 mA g^{-1}	46
KMHCF	20 M KAc gel	0–1 V *vs.* Ag/AgCl	57 mA h g^{-1}/200 mA g^{-1}	∼52.6%/400/200 mA g^{-1}	—	47
$K_{2.55}Zn_{3.08}[Fe(CN)_6]_2\cdot 0.28H_2O$	3.0 M KCF_3SO_3 + 2.0 M $Zn(CF_3SO_3)_2$	0–1.2 V *vs.* SCE	70.0 mA h g^{-1}/1000 mA g^{-1}	93.7%/10 000/20 A g^{-1}	26.5 mA h g^{-1}/30 A g^{-1}	48
PG	1 M KNO_3	0–1 V *vs.* Ag/AgCl	121.4 mA h g^{-1}/111 mA g^{-1}	44.7%/1100/500 mA g^{-1}	83.7 mA h g^{-1}/388 mA g^{-1}	49
PY/ITO	0.1 M KCl	−0.32–1.2 V *vs.* Ag/AgCl	142 mA h g^{-1}/416 mA g^{-1}	82%/500/416 mA g^{-1}	57 mA h g^{-1}/3333 mA g^{-1}	50
$Na_3V_2(PO_4)_3$	1 M K_2SO_4	−0.2 to 0.9 V *vs.* SCE	—	—	—	51
$K_{0.22}V_{1.74}O_{4.37}\cdot 0.82\ H_2O$	1 M KCl	−0.1 to 0.9 V *vs.* Ag/AgCl	183 mA h g^{-1}/5 mV s^{-1}	∼100%/5000/2 A g^{-1} (Full cell)	93 mA h g^{-1}/200 mV s^{-1}	52
$V_2O_5\cdot 0.6H_2O$	0.5 M K_2SO_4	0–1.0 V *vs.* SCE	50 mA h g^{-1}/100 mA g^{-1}	—	—	53
δ-$K_{0.5}V_2O_5$	22 M KCF_3SO_3	−0.4 to 0.8 V *vs.* SCE	116 mA h g^{-1}/100 mA g^{-1}	88.2%/1000/100 mA g^{-1}	65 mA h g^{-1}/5 A g^{-1}	54
Nb_2C	1 M KCl	−0.2 to 0.8 V *vs.* SCE	66.2 mA h g^{-1}/0.1 A g^{-1}	90.4%/20 000/5 A g^{-1}	32.7 mA h g^{-1}/5 A g^{-1}	55
Ti_2C	1 M KCl	−0.2 to 0.8 V *vs.* SCE	52.7 mA h g^{-1}/0.1 A g^{-1}	89.7%/20 000/5 A g^{-1}	26.4 mA h g^{-1}/5 A g^{-1}	55
Ti_3C_2	1 M KCl	−0.2 to 0.8 V *vs.* SCE	57.3 mA h g^{-1}/0.1 A g^{-1}	92.5%/20 000/5 A g^{-1}	21.4 mA h g^{-1}/5 A g^{-1}	55

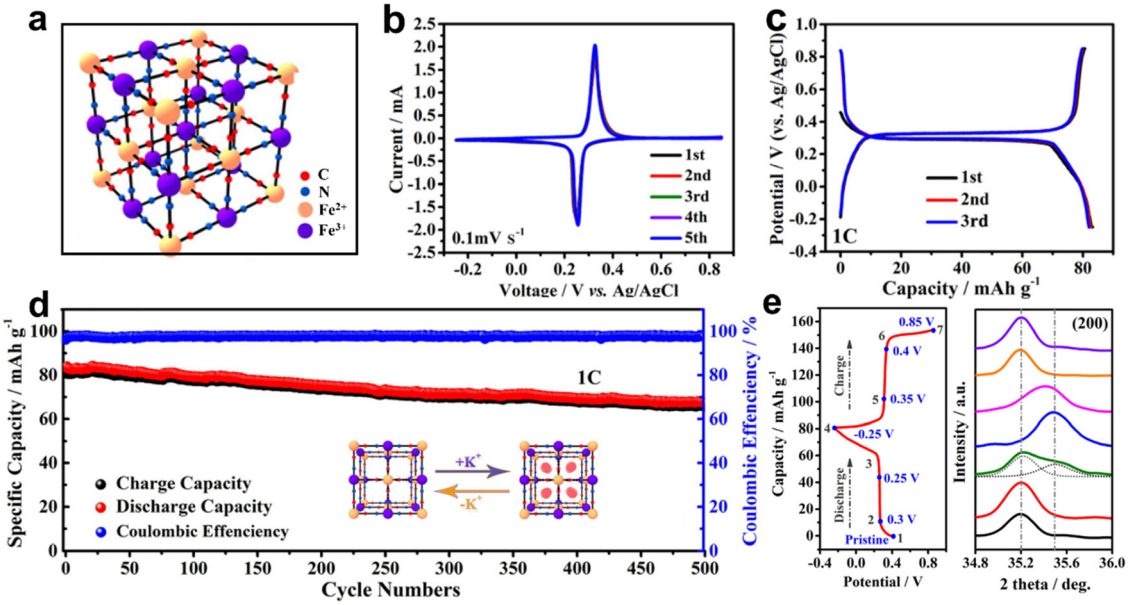

Fig. 3 (a) Crystal structure of PB. (b) CV curves and (c) GCD profiles of PB. (d) Cyclability at 1C, and (e) *ex situ* XRD patterns of PB. Reproduced with permission from ref. 29. Copyright 2020, Elsevier Inc.

nanocubes as cathode material for AKIBs.[39] The structure of this material is orthogonally symmetric rather than the usual cubic structure (Fig. 4g). Two couples of charge/discharge plateaus (0.92/0.84 and 0.3/0.2 V) appeared in the galvanostatic

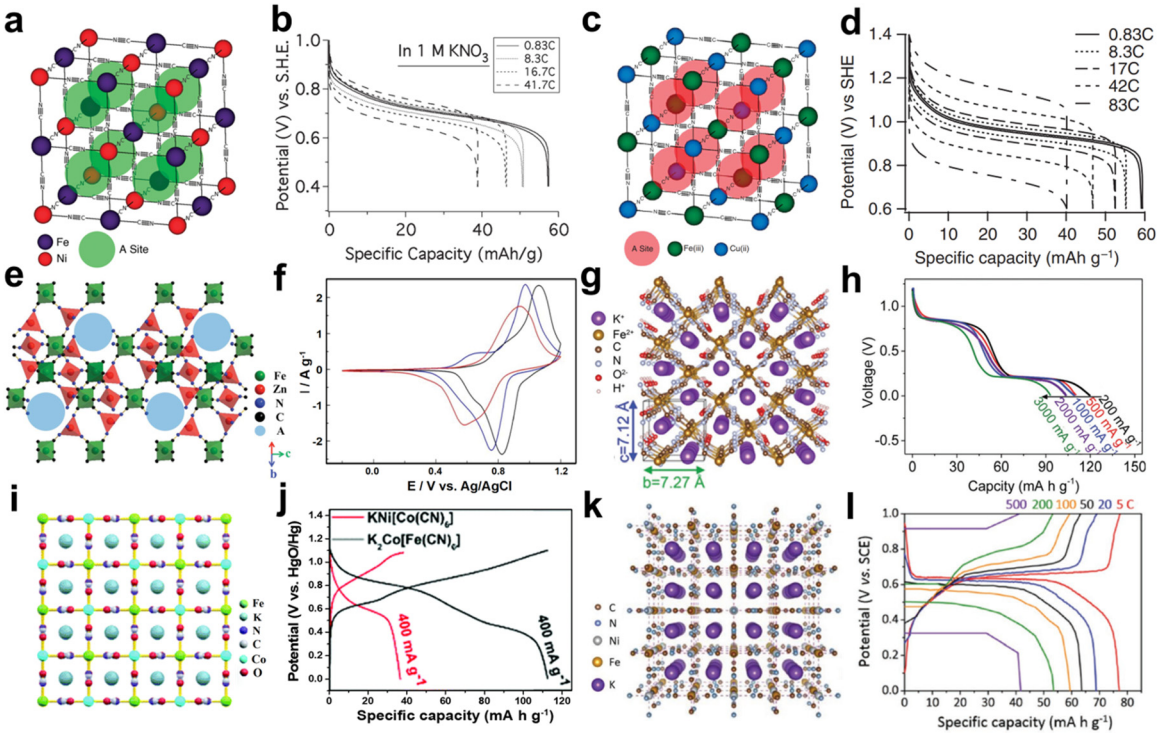

Fig. 4 (a) Crystal structure and (b) typical discharge profiles of different rates of NiHCF. Reproduced with permission from ref. 36. Copyright 2011, American Chemical Society. (c) Crystal structure and (d) discharge profiles of different rates of CuHCF. Reproduced with permission from ref. 35. Copyright 2011, Springer Nature. (e) Crystal structure and (f) CV curves in K_2SO_4 (black), Na_2SO_4 (blue), and $ZnSO_4$ (red) electrolytes of ZnHCF. Reproduced with permission from ref. 40. Copyright 2014, Wiley-VCH. (g) Crystal structure and (h) discharge profiles from 200 to 3000 mA g^{-1} of $K_2Fe^{II}[Fe^{II}(CN)_6]\cdot 2H_2O$. Reproduced with permission from ref. 39. Copyright 2016, Wiley-VCH. (i) Crystal structure of $K_2Co[Fe(CN)_6]$. (j) GCD profiles of $KNi[Co(CN)_6]$ and $K_2Co[Fe(CN)_6]$. Reproduced with permission from ref. 38. Copyright 2021, The Royal Society of Chemistry. (k) Crystal structure and (l) rate performance from 5 to 500C of $K_2NiFe(CN)_6\cdot 1.2H_2O$. Reproduced with permission from ref. 43. Copyright 2018, Wiley-VCH.

charge/discharge (GCD) in 0.5 M K_2SO_4 electrolyte, which are related to the reversible K^+ insertion/extraction. The electrode achieved a high capacity of 140 mA h g^{-1}, manifesting the reaction of two-electron transfer. Discharge capacities of 111, 109, 104, 100, and 93 mA h g^{-1} were obtained at 0.2, 0.5, 1, 2, and 3 A g^{-1}, respectively (Fig. 4h). It can be found that two-electron redox processes and high K content enabled high capacity of the electrode, and a robust open-framework structure facilitated fast kinetics of K^+. Recently, K-poor $KNi[Co(CN)_6]$ and K-rich $K_2Co[Fe(CN)_6]$ as AKIB cathodes were comparatively investigated by Chen *et al.*[38] They simulated the atomic arrangement of $K_2Co[Fe(CN)_6]$ with the square arrangement of atoms providing a large number of void sites to accommodate K^+ (Fig. 4i). $K_2Co[Fe(CN)_6]$ showed redox plateaus at 0.84/0.80 and 0.63/0.39 V, indicating two coordination sites for the intercalation/deintercalation of K^+. While $KNi[Co(CN)_6]$ demonstrated a pair of discharge/charge plateaus at 0.94/0.54 V, suggesting one coordination site for K^+ storage. Thus, $K_2Co[Fe(CN)_6]$ delivered a discharge capacity of 112 mA h g^{-1} in K_2SO_4-based electrolytes, higher than that of $KNi[Co(CN)_6]$ (37 mA h g^{-1}) (Fig. 4j). The higher capacity of $K_2Co[Fe(CN)_6]$ can be ascribed to the abundant K element, abundant active sites, and two-electron redox processes. A mesoporous K-rich nickel ferrocyanide cathode ($K_2NiFe(CN)_6{\cdot}1.2H_2O$) for ultrafast AKIBs was developed by Zhao *et al.*[43] Ni and Fe ions together with C-N bonds formed a double perovskite framework (Fig. 4k). At an ultrahigh current density of 500C, the electrode showed a high discharge capacity of 42.1 mA h g^{-1}, equivalent to 54.4% at 5C. It is worth noting that it only took 4.1 s to complete one discharge/charge cycle at 500C, which was extremely high for the rate performance reported at that time (Fig. 4l). Based on the *ex situ* Raman spectroscopy characterization, the reversible transformation of Fe^{III} and Fe^{II} during the redox process was demonstrated.

PBA compounds show controllable morphologies during preparation, and structural engineering plays an important role in promoting ion diffusion, inhibiting material dissolution, and improving electrochemical performance. Partial substitution of N-coordinated P ions with another metal ion is an efficient

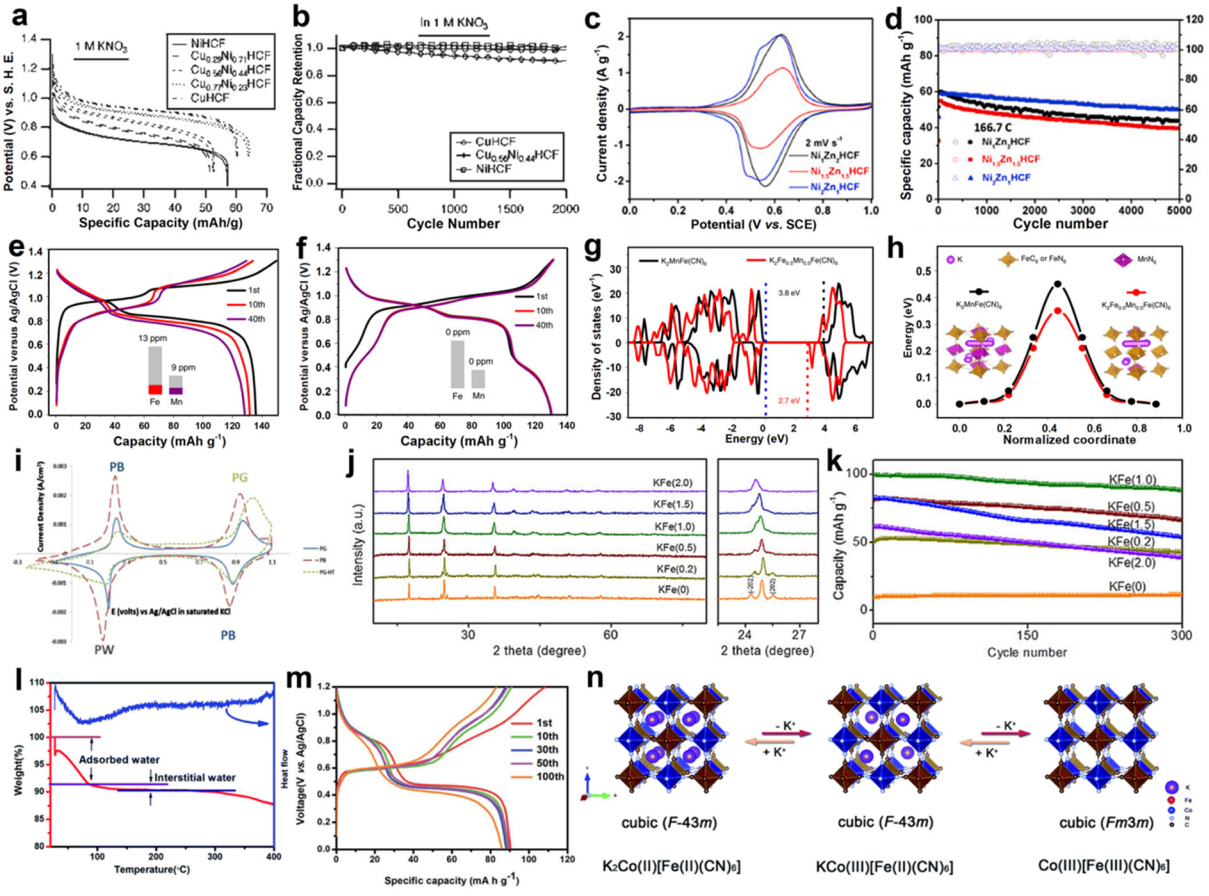

Fig. 5 (a) GCD profiles of different rates and (b) cycling performance of CuNiHCF. Reproduced with permission from ref. 37. Copyright 2012, American Chemical Society. (c) CV curves and (d) cycling performance of Ni_xZn_yHCF. Reproduced with permission from ref. 41. Copyright 2020, Elsevier Inc. GCD profiles of (e) $K_2MnFe(CN)_6$ and (f) $K_2Fe_{0.35}Mn_{0.65}Fe(CN)_6$. (g) Density of states and (h) the K^+ migration energy barriers in the $K_2Fe_{0.5}Mn_{0.5}Fe(CN)_6$ and $K_2MnFe(CN)_6$. Reproduced with permission from ref. 44. Copyright 2019, Springer Nature. (i) CV curves of PB, PG, and PG-HT electrodes in KNO_3 electrolyte. Reproduced with permission from ref. 49. Copyright 2015, Elsevier Inc. (j) XRD patterns and (k) long-term cyclability at 1500 mA g^{-1} of $K_{1.93}Fe[Fe(CN)_6]_{0.97}{\cdot}1.82H_2O$ and other samples. Reproduced with permission from ref. 42. Copyright 2018, Wiley-VCH. (l) TG/DSC curves and (m) GCD profiles of $K_2CoFe(CN)_6$. (n) Schematic illustration of the structure and valence for $K_2CoFe(CN)_6$. Reproduced with permission from ref. 45. Copyright 2020, The Royal Society of Chemistry.

strategy to influence the properties of PBAs, which has been extensively studied in organic batteries.[63,64] For example, the copper-nickel hexacyanoferrate (CuNiHCF) was synthesized by the ratio regulation of Cu to Ni in the material.[37] Ni and Cu in the CuNiHCF crystal structure formed a fully miscible solution on the P site (Fig. 5a). The reaction potential of CuNiHCF with K^+ was controllable from 0. 6 to 1.0 V by changing the content of Ni and Cu in the structure (Fig. 5b). NiHCF and CuHCF displayed 100% capacity retention after 2000 cycles, while $Cu_{0.56}Ni_{0.44}$HCF lost 9% of its initial capacity. The capacity loss of the $Cu_{0.56}Ni_{0.44}$HCF may be due to the dissolution of the electrode, and the relative concentrations of Ni and Cu also have an influence on the chemical stability of $Cu_{0.56}Ni_{0.44}$HCF. In recent work, a series of Ni_xZn_yHCF (x = 1, 1.5, or 2, y = 2, 1.5, or 1) was reported by Mai *et al.* as cathodes for AKIBs.[41] Ni_xZn_yHCF was designed by the synergistic effect between high voltage Zn^{2+} and stable Ni^{2+}. All three samples exhibited linear rigid coordination of Fe–C≡N–M (M = Ni, Zn) mechanisms to form cubic frameworks. Among them, Ni_2Zn_1HCF showed the lowest polarization and the highest redox potential in the aqueous K_2SO_4 solution revealed by the CV curves (Fig. 5c). Ni_2Zn_1HCF exhibited the average equilibrium potentials of 0.6 V *vs.* SCE and the highest capacity retention of 85.5% at 166.7C (Fig. 5d). Impressively, Ni_2Zn_1HCF exhibited an ultrahigh rate capability at 1000C with 66% capacity retention and ultralong life span of 80 000 cycles with 0.000385% capacity decay per discharge/charge cycle at 1000C. Such excellent performance was associated with the mechanism of near-pseudocapacitive intercalation, the large surface area, and the structural stability brought by the high Ni content. Hu *et al.* explored the electrochemical stability of K-rich $K_2MnFe(CN)_6$ affected by Fe substitution.[44] They found that Mn ions replaced by the proper amount of Fe ions could effectively inhibit the dissolution of the material in the aqueous electrolyte during the discharge/charge process (Fig. 5e and f). Thus, the optimal K-rich sample, $K_2Fe_{0.35}Mn_{0.65}Fe(CN)_6$, achieved a high capacity of 135 mA h g^{-1} and high-rate performance with 5% capacity loss at 20C. In this regard, Fe substitution not only reduces the density of Mn^{3+} in the lattice, but also significantly changes the Mn^{2+}/Mn^{3+}–N redox reaction mechanism. Based on first principles calculations, $K_2Fe_{0.5}Mn_{0.5}Fe(CN)_6$ showed small band gap and low K^+ ion diffusion energy when compared with that of $K_2MnFe(CN)_6$, suggesting the improved electronic conductivity and K^+ diffusion dynamics (Fig. 5g and h).

In addition to the strategy of partial substitution, reducing grain size, increasing crystallinity, and reducing defects are also used to improve the electrochemical stability of PBAs. Very recently, Padigi and co-workers synthesized PB and Prussian green (PG) using different precursors (potassium ferricyanide and potassium ferrocyanide) as AKIB cathodes in KNO_3-based electrolyte.[49] Different precursors induced different reaction rates, resulting in much smaller PG particles (50–75 nm) than PB particles (2–10 μm). As revealed by the CV curves, the insertion and extraction of K^+ were highly reversible for PG (Fig. 5i). K^+ first intercalated at 0.89 V to form PB, and then K^+ continued to intercalate at 0.2 V to generate Prussian white (PW). Compared to PG, PB exhibited similar K^+ storage behavior. However, the specific capacity of PG exhibited a significant increase from 53 to 121 mA h g^{-1} compared with PB. This is due to the smaller particle size resulting in a shorter diffusion length for K^+. Additionally, Li and co-workers synthesized a series of PW with different particle sizes and crystallinities by adjusting the acidity of hydrothermal conditions.[42] As the increase of the concentration of hydrochloric acid, the structure of the material gradually transformed from the monoclinic phase of KFe (0) to the cubic phase of KFe (2.0), and the gradually broadened half-peak width indicated the decreased grain size of the material (Fig. 5j). When used as cathodes for AKIBs, KFe (1.0) electrode exhibited the highest capacity of 142 mA h g^{-1} at 75 mA g^{-1} and good stability with 88% capacity retention over 300 cycles at 1.5 A g^{-1} (Fig. 5k). The high crystallinity of the electrode alleviated its continuous dissolution in an aqueous solution, and the reduced grain size enhanced the ion diffusion kinetics, which synergistically improves the K^+ storage stability. Moreover, Jiao *et al.* synthesized low-defect $K_2CoFe(CN)_6$ (CoHCF) using a coprecipitation method and investigated it as a cathode for AKIBs.[45] CoHCF showed low water content of less than 10%, indicating low crystalline defects in the sample (Fig. 5l). The CV curves of the electrode demonstrated two pairs of redox peaks, suggesting the existence of two-electron transfer during the electrochemical process. It can deliver a high discharge capacity of 83.6 mA h g^{-1} at 20 mA g^{-1} in KCF_3SO_3-based electrolytes (Fig. 5m). Low defects could avoid the block of active sites, the inhibition of ion transport, and the reduction of electrochemical activity of P sites. During K^+ intercalation/deintercalation, a solid solution reaction between $K_2Co(II)Fe(II)(CN)_6$ and $KCo(III)Fe(II)(CN)_6$ in the low voltage range, and a phase transformation from $F\bar{4}3m$ to $Fm3m$ in the high voltage range were confirmed (Fig. 5n).

Apart from the above-mentioned improvement strategies, growing active materials on conductive substrates is also a useful strategy to enhance the electrochemical performance.[65] For example, the Prussian yellow (PY) film on indium tin oxide (ITO) substrate was reported by Baioun and colleagues, and the obtained composite material exhibited superior electrochemical performances.[50] A high capacity of 142 mA h g^{-1} and high capacity retention of 82% were demonstrated at 3C for 500 cycles, manifesting its good cycling stability. When this cathode material was assembled with the Zn anode to form a full cell, it achieved a high output potential of 1.9 V, indicating the promising application in AKIBs.

Recent research has demonstrated that PB and PBAs are promising K^+ storage cathode materials due to their open framework, high voltage platform, simple preparation, and low cost. However, some challenges in practical applications still exist for PB and PBAs, which suffer from poor rate performance and fast capacity fading caused by low electronic conductivity, interstitial or coordinated water, excess lattice defects, and complex side reactions with electrolytes. Fortunately, a series of effective strategies have been adopted to modify the electrochemical property of these cathode compounds, including metal ion substitution or doping, particle size reduction, crystallinity enhancement, defect reduction, and conducting

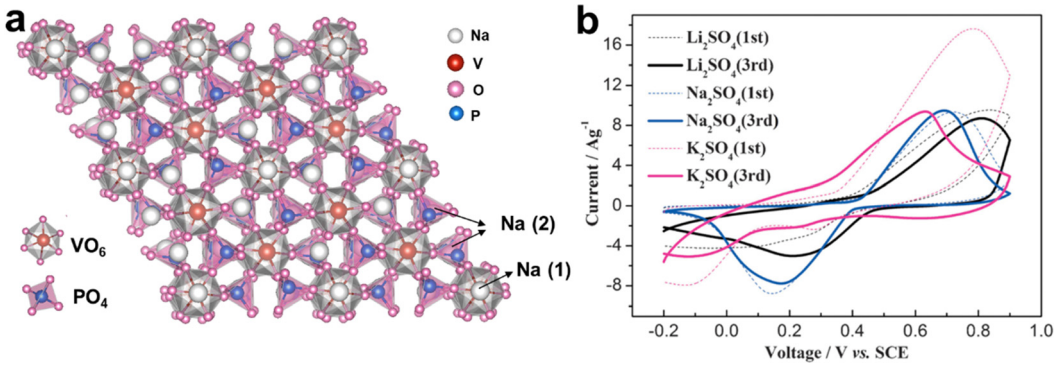

Fig. 6 (a) Crystal structure of $Na_3V_2(PO_4)_3$. (b) CV curves of $Na_3V_2(PO_4)_3$ at 5 mV s^{-1} in 1 M K_2SO_4, Na_2SO_4, and Li_2SO_4 electrolytes. Reproduced with permission from ref. 51. Copyright 2014, Wiley-VCH.

modification.[66] Therefore, it is necessary to optimize the lattice structures through feasible structural design strategies, so that the electrode material can store K^+ reversibly with high efficiency, and the cycle stability is not affected by unfavorable factors.

2.1.2. Polyanionic compounds. Polyanionic compounds hold potential as cathodes for LIBs and sodium-ion batteries (SIBs) because they show high output voltage, robust three-dimensional frameworks, fast ions conductivity, and abundant vacancies.[67] For example, $Na_3V_2(PO_4)_3$ is a representative NASICON type cathode, which shows larger channels to accommodate Na^+.[68–70] As early as 2014, Ji *et al.* discovered the electrochemical behavior of $Na_3V_2(PO_4)_3$ in K_2SO_4, Na_2SO_4, and Li_2SO_4 electrolytes.[51] As shown in Fig. 6a, the crystal structure of $Na_3V_2(PO_4)_3$ consists of VO_6 octahedra and corner-sharing PO_4 tetrahedra with two Na sites, namely Na(1) and Na(2). This robust crystal structure allows $Na_3V_2(PO_4)_3$ to allow insertion/extraction of alkali metal ions. The large polarization during the first three charge-discharges occurred in K_2SO_4 and Li_2SO_4 electrolytes, indicating the limited electroactivity of $Na_3V_2(PO_4)_3$ in the two electrolytes (Fig. 6b). The presence of these asymmetric redox peaks indicated that the electrochemical intercalation/deintercalation processes of K^+ and Li^+ were believed to be irreversible. The K^+ storage mechanism may be the formation of electrochemical double-layer capacitance (EDLC) on the surface rather than being embedded in the bulk, which is due to the weakest solvation of K^+, the smallest charge density, and the higher conductivity. This may explain why $Na_3V_2(PO_4)_3$ exhibited more capacity in Na_2SO_4 electrolytes than in K_2SO_4 electrolytes.

In brief, polyanionic compounds are highly promising for high-energy AKIBs owing to their stable framework, high voltage, and high thermal stability. Compared with PB and PBAs, the relatively high density of polyanions makes them promising AKIB cathode materials. Although low electronic conductivity is a disadvantage that cannot be ignored, it can be well modified by nanocomposite design, carbon coating, the alkali ions partially substitution or other effective strategies. Therefore, the development of high-capacity polyanionic compounds is a promising research direction. Especially, through the investigation of new polyanion materials and structural engineering, the K^+ storage capacity of such materials can be further improved.

2.1.3. Vanadium-based oxides. Vanadium-based materials, especially layered vanadium oxides, have attracted enormous interest in aqueous alkaline ion batteries due to their large interlayer spacing and multiple valence states.[71–76] The open interlayer provides diffusion channels for alkali metal ions, and the abundant valence changes of vanadium ensure high specific capacity. Therefore, Vanadium-based oxides materials are another type important cathode materials for AKIBs.

Wu and co-workers investigated the electrochemical behavior of $V_2O_5{\cdot}0.6H_2O$ in aqueous solutions containing three alkali metal sulfates (K_2SO_4, Na_2SO_4, and Li_2SO_4).[53] The GCD profiles within 0–1 V (*vs.* SCE) exhibited a capacitor-type linear relationship (Fig. 7a). Interestingly, the specific capacity of $V_2O_5{\cdot}0.6H_2O$ to storage K^+ (50 mA h g^{-1}) exceeded those of Li^+ (37 mA h g^{-1}) and Na^+ (43 mA h g^{-1}). Meanwhile, the charge-transfer resistance (R_{ct}) value of $V_2O_5{\cdot}0.6H_2O$ in K_2SO_4 electrolyte (2.4 Ω) was smaller than those in Na_2SO_4 (3.5 Ω) and Li_2SO_4 (6.1 Ω) solutions (Fig. 7b). The fast charge transfer dynamic in the K_2SO_4 solution validated the optimal electrochemical performance. In addition, the structural evolution of $V_2O_5{\cdot}0.6H_2O$ during intercalation/deintercalation of $Li^+/Na^+/K^+$ was presented (Fig. 7c). Compared with Li^+ and Na^+, the K^+ insertion/extraction in the $V_2O_5{\cdot}0.6H_2O$ interlayer was more feasible, which could be related to the moderate charge density of K^+. However, $V_2O_5{\cdot}0.6H_2O$ showed the rapid decay of capacity in the three electrolytes.

Pre-intercalation of alkali metal ions between the layers of V_2O_5 is a typical effective strategy to improve electrochemical performance. Teng *et al.* synthesized K-intercalated disordered vanadium oxide ($K_{0.22}V_{1.74}O_{4.37}{\cdot}0.82H_2O$) as AKIB cathode.[52] The electrode exhibited a bilayer structure that is composed of [VO_6] octahedral units, and K^+ and H_2O existed between the V–O layers (Fig. 7d). When used as K^+ storage cathode, $K_{0.22}V_{1.74}O_{4.37}{\cdot}0.82H_2O$ possessed a higher capacity of 183 mA h g^{-1} at 5 mV s^{-1} and higher rate performance than those of the commercial V_2O_5 material and PEDOT:PSS (Fig. 7e). Such good electrochemical stability was due to the strong coherence between the interlayer water and the V–O layer (Fig. 7f). In addition, the highly disordered nature of the material lowered the energy barrier for K^+ transport. The synergistic effect endowed electrodes with high specific capacity and excellent rate performance. Similarly, Zhi *et al.* reconstructed α-V_2O_5 crystals into δ-$K_{0.5}V_2O_5$ bronzes

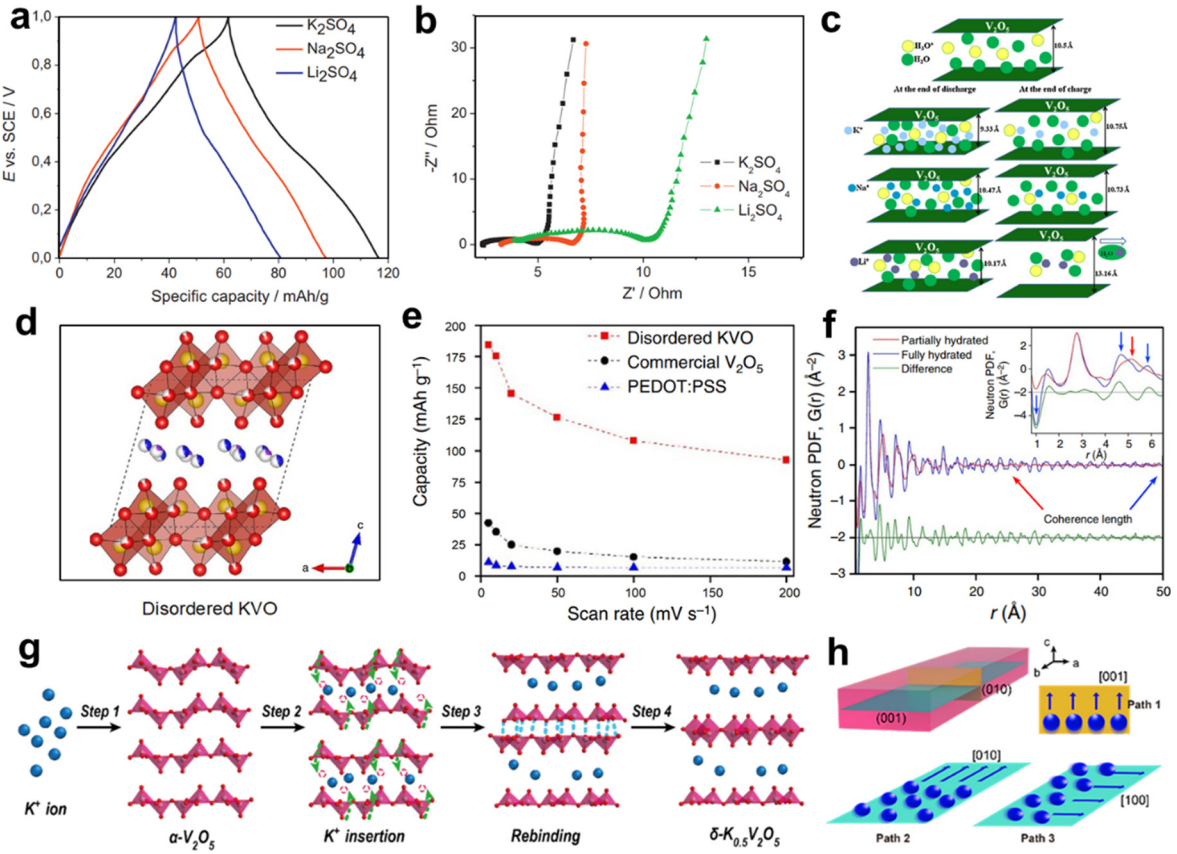

Fig. 7 (a) GCD profiles at 100 mA g^{-1} and (b) Nyquist impedance plots of $V_2O_5{\cdot}0.6H_2O$ in K_2SO_4, Na_2SO_4, and Li_2SO_4 electrolytes. (c) Schematic illustration of structural evolution of $V_2O_5{\cdot}0.6H_2O$ in three electrolytes. Reproduced with permission from ref. 53. Copyright 2013, Elsevier Inc. (d) Crystal structure and (e) rate capability of disordered $K_{0.22}V_{1.74}O_{4.37}{\cdot}0.82H_2O$. (f) Neutron PDFs of disordered $K_{0.22}V_{1.74}O_{4.37}{\cdot}0.82H_2O$. Reproduced with permission from ref. 52. Copyright 2017, Springer Nature. Schematic illustration of (g) the reconstructing process from α-V_2O_5 to δ-$K_{0.5}V_2O_5$ and (h) three possible pathways for K^+ of δ-$K_{0.5}V_2O_5$. Reproduced with permission from ref. 54. Copyright 2021, American Chemical Society.

for K^+ storage.[54] The intercalated K^+ was located between the V–O layers (Fig. 7g). The structural reconstructing strategy allowed the creation of more available K^+ sites for δ-$K_{0.5}V_2O_5$. At the same current density, the δ-$K_{0.5}V_2O_5$ achieved a capacity of 116 mA h g^{-1}, while α-V_2O_5 only showed a capacity of 17 mA h g^{-1}. For δ-$K_{0.5}V_2O_5$, three possible transport pathways for K^+ in the (010) and (001) planes were suggested, and theoretical calculations demonstrated that the anisotropic storage mode of K^+ in converges to the interlayer channel along the [100] direction was the dominant path for K^+ (Fig. 7h).

To sum up, vanadium oxide and its derivatives are promising compounds in the field of AKIBs owing to multivalent and open frame structures. In general, vanadium-based materials exhibit both high specific capacity and good cycle stability. Their layered structure facilitates the reversible K^+ intercalation/deintercalation. Nevertheless, the synthesis of materials requires strict hydrothermal conditions and high-temperature annealing, which hinders the commercialization to a certain extent. Furthermore, more research works should be paid on the regulation of interlayer spacing, the deployment of structural water, and defect engineering to improve the performance of such materials.

2.1.4. MXenes. MXenes have attracted increasing research interest as a new class of two-dimensional transition metal carbides, nitrides, and carbonitrides.[77–82] Similar to other layered materials, MXenes show large and tunable interlayer spacing. Furthermore, MXenes exhibit several unique properties: (1) high electrical conductivity, (2) abundant surface chemistries (*e.g.*, –OH, –O, and –F), and (3) excellent hydrophilicity. These excellent physicochemical properties make them attractive in energy storage systems such as batteries and supercapacitors.

Recently, the exploration of MXenes (Nb_2C, Ti_2C, and Ti_3C_2) for aqueous K^+ storage was reported by Zhi's group.[55] It is well known that MXenes are a huge family of which more than 30 have been synthesized so far.[78] The crystal structure of MXene is a hexagonal close-packed structure, in which the C atoms are located in the octahedral gap. These three MXene species are typical layered structures with interlayer spacing of around 10 Å, which provides enough space for the transport of K^+ ions (Fig. 8a–c). As AKIB cathodes, high discharge capacities of 66.2 mA h g^{-1} for Nb_2C, 52.7 mA h g^{-1} for Ti_2C, 57.3 mA h g^{-1} for Ti_3C_2 at 0.1 A g^{-1} and fast K^+ transport kinetics at 5 A g^{-1} were displayed (Fig. 8d–f). No obvious plateaus in the GCD profiles are ascribed to the existence of pseudocapacitance. In addition, long-term cycling performance of the three cathodes with high capacity retentions was demonstrated. Based on *ex situ* XRD, Raman, and XPS characterizations, a highly reversible

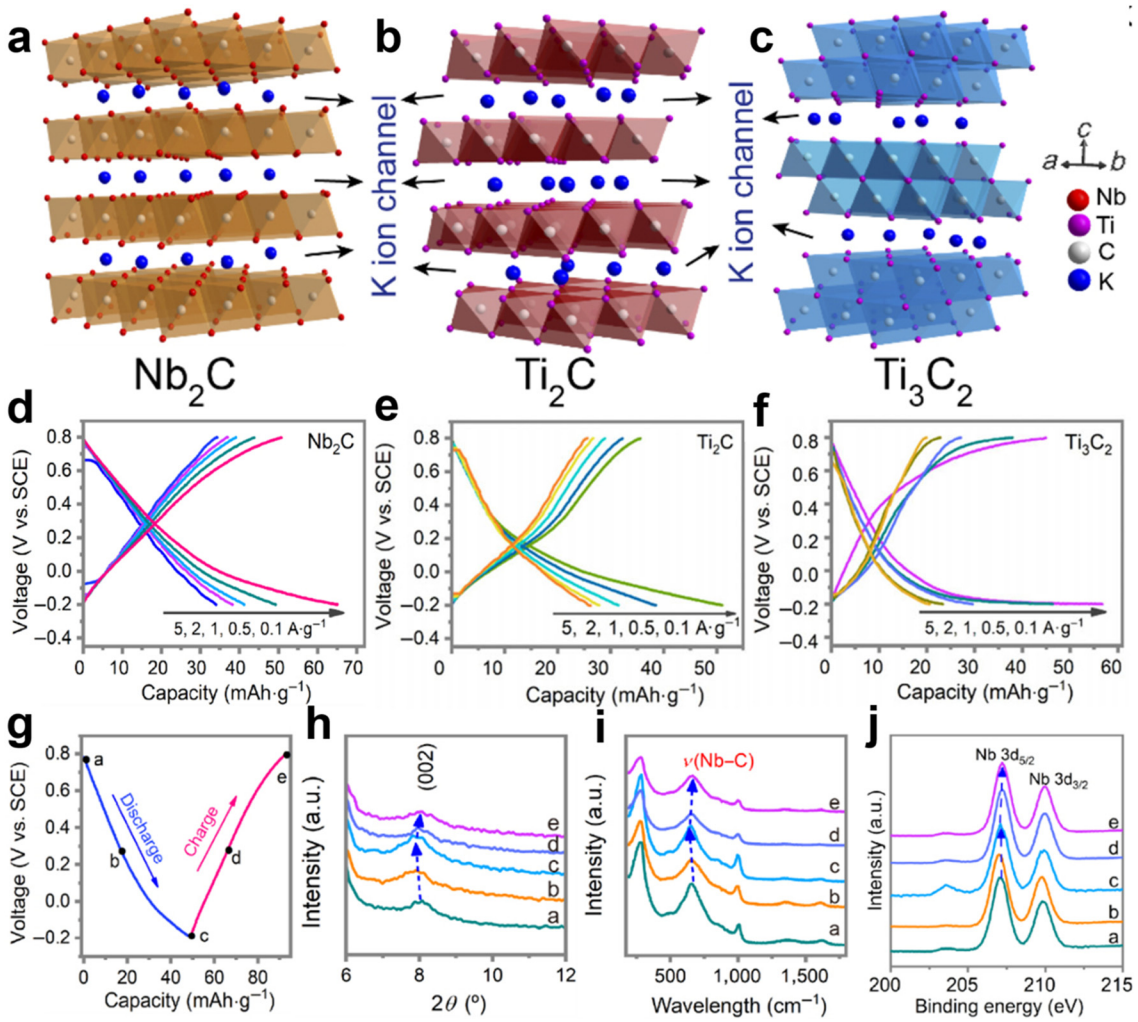

Fig. 8 Crystal structures of (a) Nb_2C, (b) Ti_2C, and (c) Ti_3C_2. GCD profiles at different rates for (d) Nb_2C, (e) Ti_2C, and (f) Ti_3C_2. (g) GCD curves of Nb_2C cathode at 0.5 A g^{-1}. The corresponding (h) XRD, (i) Raman, and (j) XPS data during the cycling. Reproduced with permission from ref. 55. Copyright 2022, Tsinghua University Press.

intercalation/deintercalation mechanism accompanied by only 1.8% variation of the Nb_2C electrode was revealed (Fig. 8g–j).

It should be pointed out that the research work on MXenes in aqueous K^+ storage is still in its infancy, and the above literature shows that MXenes are a class of promising electrode materials for emerging AKIBs. Due to the large interlayer spacing and good electrical conductivity, MXene nanostructures deserve attention in future energy storage. More interesting works are expected to emerge as synthesis methods and improvement strategies continue to advance.

2.2. Anode materials

Although several typical cathode materials have demonstrated good K^+ storage capacity so far, AKIB full cells are still infant, as their energy/power density and durability are also affected by anode materials. Since potassium metal cannot be directly used as the anode of AKIB, in order to meet the needs of rocking-chair batteries, the development of anode materials is equally important. This section will present the latest developments in AKIB anodes (Table 2). Examples of anode materials include NASICON-type materials, metal oxides/sulfides, alloy materials, and organic compounds.

2.2.1. Titanium phosphate. Although many titanium-based materials are considered to be potential anode materials for organic KIBs, only $KTi_2(PO_4)_3$ has been reported as a potential anode for AKIBs.[97,98] The $KTi_2(PO_4)_3$ structural framework is composed of PO_4 tetrahedra and TiO_6 octahedra, and K^+ completely occupies the interstitial sites (Fig. 9a). The 3D framework with large interstitial space could facilitate the rapid transmission of K^+. Ji *et al.* first examined the reversible electrochemical behavior of $KTi_2(PO_4)_3$ for K^+ storage in water-in-salt (WiSE) electrolytes.[84] CV curves revealed that the $KTi_2(PO_4)_3$ electrode exhibited a pronounced HER cathodic current in dilute electrolytes and reversible redox behavior in 30 M KAc electrolyte (Fig. 9b). Furthermore, the $KTi_2(PO_4)_3$ electrode exhibited a smaller potential hysteresis (~0.3 V) in the WiSE electrolyte than the non-aqueous system (~0.5 V), indicating more efficient kinetics in the aqueous electrolyte (Fig. 9c). Redox peaks at −1.3/

Table 2 Summary of anode materials and the corresponding electrochemical performance of AKIBs

Anode materials	Electrolyte	Working potential range	Specific capacity/current	Capacity retention/cycles/current	Rate capability/current	Ref.
$KTi_2(PO_4)_3$/C	21 M KCF_3SO_3	−1.1 to 0 V *vs.* SCE	78 mA h g^{-1}/50 mA g^{-1}	~100%/40/0.05 A g^{-1}	47.5 mA h g^{-1}/2 A g^{-1}	83
$KTi_2(PO_4)_3$	30 M KAc	−1.5 to −0.3 V *vs.* Ag/AgCl	~58 mA h g^{-1}/0.1 A g^{-1}	69%/11 000/1 A g^{-1}	~12 mA h g^{-1}/5 A g^{-1}	84
$KTi_2(PO_4)_3$	40 M HCOOK	−1.5 to −0.3 V *vs.* Ag/AgCl	~21 mA h g^{-1}/100 mA g^{-1}	—	—	85
$KTi_2(PO_4)_3$@C	2 M KFSI DMF/H_2O	−1.5 to 0 V *vs.* SCE	76 mA h g^{-1}/1 A g^{-1}	~80%/10 000/1 A g^{-1} (full cell)	33 mA h g^{-1}/20 A g^{-1} (Full cell)	86
$K_{0.36}(H_2O)_yWS_2$	0.5 M K_2SO_4	−0.8 to 0.4 V *vs.* Ag/AgCl	43.3 mA h g^{-1}/0.2 A g^{-1}	48.9%/250/0.5 A g^{-1}	25.7 mA h g^{-1}/5 A g^{-1}	87
$K_{0.38}(H_2O)_{0.82}MoS_2$	0.5 M K_2SO_4	−0.8 to 0.4 V *vs.* Ag/AgCl	~57 mA h g^{-1}/500 mA g^{-1}	48.5%/500/5 A g^{-1}	~40 mA h g^{-1}/8 A g^{-1}	88
α-MoO_3@TiO_2	0.5 M KPF_6	0.05–1 V (Coin cell)	41.27 mA h g^{-1}/5C	66.2%/20/5C	—	89
$K_xV_2O_5{\cdot}nH_2O$	0.5 M K_2SO_4	−0.8 to 0 V *vs.* Ag/AgCl	382 mA h g^{-1}/5 mV s^{-1}	80%/10 000/500 mV s^{-1} (full cell)	81 mA h g^{-1}/1000 mV s^{-1}	90
Mo-based	0.1 M KCl	−0.2 to 0.4 V *vs.* Ag/AgCl	517 mA h g^{-1}/7 A g^{-1}	—	~60 mA h g^{-1}/112 A g^{-1}	91
Bi	1 M KOH	−1.2 to 0 V *vs.* SCE	254.3 mA h g^{-1}/28.8 mA g^{-1}	88.8%/1600/0.57 A g^{-1}	147.3 mA h g^{-1}/8.768 A g^{-1}	92
Bi	1 M KOH	−1.2 to 0 V *vs.* SCE	~226 mA h g^{-1}/0.2 A g^{-1}	76.6%/2000/1 A g^{-1}	220 mA h g^{-1}/8 A g^{-1}	93
β-PTCDA	30 M KFSI	−1.1 to 0.1 V *vs.* SCE	145 mA h g^{-1}/200 mA g^{-1}	82%/500/2 A g^{-1}	120.4 mA h g^{-1}/8 A g^{-1}	94
PNTCDA	3.75 M KNO_3	−1.0 to −0.2 V *vs.* SCE	135 mA h g^{-1}/360 mA g^{-1}	~79%/300/360 mA g^{-1}	93.2 mA h g^{-1}/5400 mA g^{-1}	95
PTCDI	22 M KCF_3SO_3	−1.3 to 0.3 V *vs.* Ag/AgCl	125 mA h g^{-1}/65 mA g^{-1}	77%/1000/2.6 A g^{-1}	110 mA h g^{-1}/2.6 A g^{-1}	44
PAQS	10 M KOH	−1.0 to 0.1 V *vs.* SHE	200 mA h g^{-1}/100 mA g^{-1}	88%/1350/200 mA g^{-1}	186 mA h g^{-1}/2250 mA g^{-1}	96

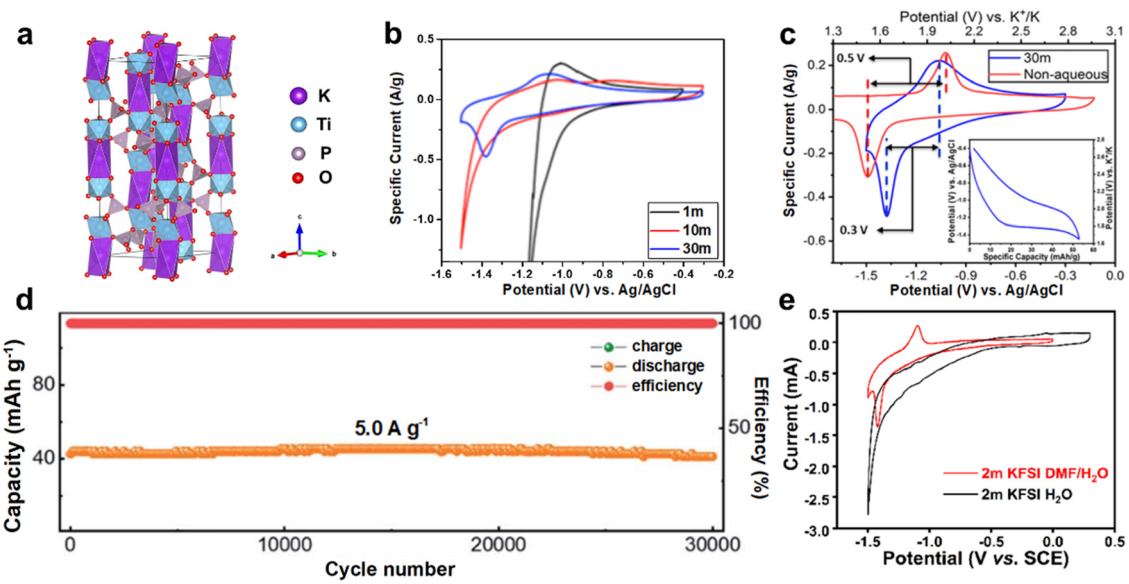

Fig. 9 (a) Crystal structure of $KTi_2(PO_4)_3$. (b) CV curves of $KTi_2(PO_4)_3$ in different concentration KAc electrolytes at 0.5 mV s^{-1}. (c) CV curves of $KTi_2(PO_4)_3$ in aqueous and nonaqueous electrolytes. Reproduced with permission from ref. 84. Copyright 2018, American Chemical Society. (d) Long-term cycling performance of AKIB full cell consisted of K-FeHCF cathode and $KTi_2(PO_4)_3$/C anode at 5.0 A g^{-1}. Reproduced with permission from ref. 83. Copyright 2021, Royal Society of Chemistry. (e) CV curves of $KTi_2(PO_4)_3$@C in 2 M KFSI electrolytes with and without DMF. Reproduced with permission from ref. 86. Copyright 2021, American Chemical Society.

−1.0 V *vs.* Ag/AgCl were observed, revealing the redox conversion between Ti^{3+} and Ti^{4+}. However, the $KTi_2(PO_4)_3$ electrode showed a low capacity of 53 mA h g^{-1} and poor rate performance.

As an easy-to-handle technology, carbon coating or carbon composites shows great advantages in enhancing the electronic conductivity of anode materials. Recently, Li *et al.* synthesized $KTi_2(PO_4)_3$/C nanoparticles that showed rapid delivery of K^+.[83] A full cell with $KTi_2(PO_4)_3$/C anode, iron hexacyanoferrate ($K_2FeFe(CN)_6$) cathode, and 21 M KCF_3SO_3 WiSE electrolyte was constructed. The full cell achieved a discharging capacity of 73 mA h g^{-1} (based on $KTi_2(PO_4)_3$/C anode) and an average discharge potential of 1.5 V. Even at 5 A g^{-1}, the AKIB full cell exhibited little capacity loss of 3.3% after 30 000 cycles (Fig. 9d). Besides, the $KTi_2(PO_4)_3$/C showed fast reaction kinetics and

maintained near-zero strain during K^+ storage, thus achieving excellent performance.

To further enhance the electrochemical performance of $KTi_2(PO_4)_3$@C, electrolyte additives are adopted. A hybrid electrolyte based on KFSI was designed by Li *et al.*[86] DMF was introduced into the KFSI dilute electrolyte, which not only broadened the ESW of the electrolyte, but also modified the cycling stability of the electrode. Using 2 M KFSI DMF/H_2O electrolyte, the $KTi_2(PO_4)_3$@C anode exhibited distinct redox peaks in the CV curves, while almost no peaks were observed when using 2 M KFSI aqueous electrolyte (Fig. 9e). Therefore, the hybrid electrolyte stimulated the electrochemical activity of the $KTi_2(PO_4)_3$@C due to the presence of DMF. Moreover, after 200 cycles, the $KTi_2(PO_4)_3$@C anode showed a high capacity of 76 mA h g^{-1}, indicating its good cycling stability.

In summary, titanium phosphate is still an ideal anode for AKIBs due to its small volume change during K^+ storage, relatively good cycling stability, and nontoxicity. Note that the main drawbacks of titanium phosphate as anode for AKIBs are unsatisfactory discharge capacity and rate capability. Therefore, further improvements in capacity, cyclability, and rate performance are urgently needed. The optimization strategies, such as carbon coating, hybrid composites, and electrolyte engineering, are promising for the high performance of AKIBs.

2.2.2 Metal oxides/sulfides. Conversion anodes have been widely used in organic battery systems thanks to their high capacity, environmental friendliness, and low cost.[99–102] The latest reported conversion anodes for AKIBs are transition metal oxides and dichalcogenides.

Since Dahn *et al.* first used VO_2 as an anode for aqueous LIBs in 1994, other vanadium-based electrode materials have been developed as anodes for AKIBs.[8] Jiang *et al.* designed amorphous/crystalline $K_{0.25}V_2O_5{\cdot}nH_2O$/*o*-$V_2O_5$ dual phases (ac-$K_xV_2O_5$) anode for aqueous K^+ micro-batteries (AKMBs).[90] Amorphous $K_{0.25}V_2O_5{\cdot}nH_2O$ acted as a molecular pillar between layers, which not only enabled ac-$K_xV_2O_5$ to possess new accommodation sites and ion diffusion paths, but also maintained the larger interfacial spacing of crystalline V_2O_5 bilayers (Fig. 10a). Such nanostructure was beneficial for the hydrated K^+ intercalation/de-intercalation in ac-$K_xV_2O_5$, whereas the K^+-free ac-V_2O_5 was unfavorable for K^+ storage, due to narrow interlayer spacing, sluggish diffusion kinetics, and drastic volume changes. Compared to c-$K_xV_2O_5$ and a-$K_xV_2O_5$, the capacity of ac-$K_xV_2O_5$ was significantly improved due to its biphasic nanostructure, which provided more space for hydrated K^+ and promoted K^+ diffusion kinetics between layers (Fig. 10b). When coupled with the c-K_xMnO_2 cathode, the full microcells possessed a wide working voltage window of 1.6 V.

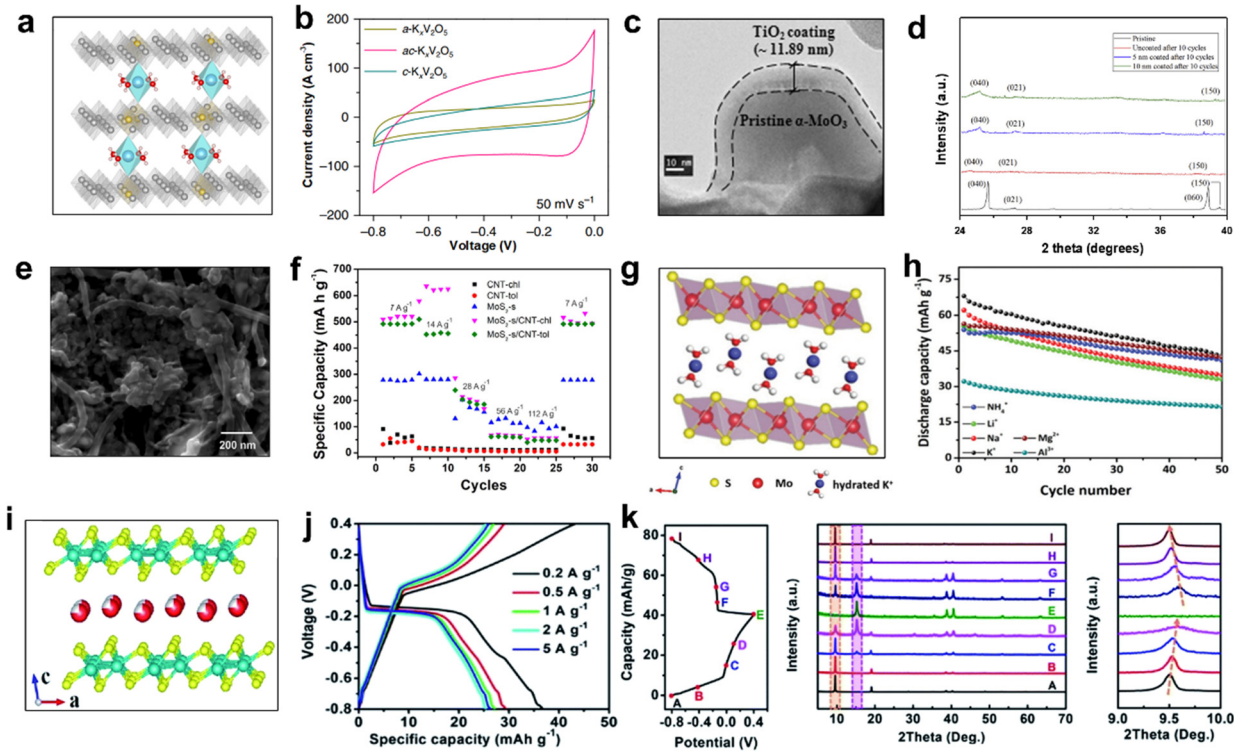

Fig. 10 (a) Crystal structure of ac-$K_xV_2O_5$. (b) CV curves of a-$K_xV_2O_5$, ac-$K_xV_2O_5$, and c-$K_xV_2O_5$. Reproduced with permission from ref. 90. Copyright 2019, Springer Nature. (c) TEM image of α-MoO_3 with TiO_2 coating. (d) XRD patterns of α-MoO_3 samples with and without coating after cycles. Reproduced with permission from ref. 89. Copyright 2016, Elsevier Inc. (e) SEM image of MoS_2-s/CNT-chl. (f) Rate performance of CNT and Mo-based samples. Reproduced with permission from ref. 91. Copyright 2021, Elsevier Inc. (g) Crystal structure and (h) cycling performance with different cations at 0.5 A g^{-1} of $K_{0.38}(H_2O)_{0.82}MoS_2$. Reproduced with permission from ref. 88. Copyright 2020, The Royal Society of Chemistry. (i) Crystal structure, (j) GCD profiles at different current densities, and (k) *ex situ* XRD patterns of $K_{0.36}(H_2O)_yWS_2$. Reproduced with permission from ref. 87. Copyright 2019, The Royal Society of Chemistry.

Stable cyclability with ~80% capacity retention over 10 000 cycles was maintained at 500 mV s^{-1}. Besides, the volumetric energy density (~103 mW h cm^{-3}) and power density (~600 W cm^{-3}) of AKMB far exceeded most reported aqueous systems at that time.

Molybdenum (Mo)-based materials (such as MoO_3 and MoS_2) have been studied extensively as the intercalation anodes for LIBs and SIBs.[103,104] Park *et al.* demonstrated the effect of material strain on α-MoO_3 anode for AKIBs with TiO_2 film deposited on the surface using the *ex situ* XRD method.[89] The TiO_2 layer was 11 nm thick after 10 nm ALD deposition, confirming the approximate coating thickness applied (Fig. 10c). The XRD patterns of α-MoO_3 and α-MoO_3 coated with 5 nm and 10 nm TiO_2 after 10 discharge/charge cycles revealed the improved structure stability with the increase of TiO_2 coating thickness (Fig. 10d). As a result, the 10 nm-coated sample exhibited the highest capacity retention, attributed to the low strain at the interface of amorphous TiO_2/crystalline α-MoO_3. Moreover, Zarbin *et al.* prepared several Mo-based/carbon nanotube (CNT) nanocomposites by a simple liquid/liquid interfacial route (LLIR)-based method.[91] It can be noticed that MoS_2 and CNT-chl mixed homogeneously (Fig. 10e). Most of the GCD profiles showed plateaus at 0.1 V, indicating that K^+ was intercalated in MoS_2 bulk. The ultrahigh specific capacity of 517 mA h g^{-1} made it promising for AKIBs (Fig. 10f). In addition, Huang *et al.* discovered that the hydrated Mo-based ternary sulfide $K_{0.38}(H_2O)_{0.82}MoS_2$ reversibly stored a variety of hydrated cations (K^+, Li^+, Na^+, Mg^{2+}, Al^{3+}, NH_4^+).[88] Similar to 2H MoS_2, $K_{0.38}(H_2O)_{0.82}MoS_2$ exhibits a typical layered structure, but the intercalation of hydrated K^+ increases the interlayer spacing from 6.2 Å to 9.3 Å (Fig. 10g). The higher electrical conductivity of $K_{0.38}(H_2O)_{0.82}MoS_2$ is due to the presence of twisted [MoS_6] octahedra in the [Mo–S] layer. The redox peaks of CV curves were mainly located between −0.4 and 0.4 V. Interestingly, $K_{0.38}(H_2O)_{0.82}MoS_2$ possessed a discharge capacity of ~68 mA h g^{-1} for K^+ storage, which exceeded other guest ions (Fig. 10h). Based on the results of *ex situ* XRD and XPS characterizations, a typical two-phase reaction mechanism was revealed, with the first phase transition between $K_{0.38}(H_2O)_{0.82}MoS_2$ and 1T′ MoS_2, followed by the reversible intercalation and deintercalation between 1T′ MoS_2 and $A_x(H_2O)_yMoS_2$.

Tungsten disulfide (WS_2) has also been regarded as a promising electrode material due to the large lattice spacing of 6.2 Å and the weak van der Waals interactions.[105] Recently, Huang *et al.* synthesized $K_{0.36}(H_2O)_yWS_2$ layered compound as a novel anode material for AKIBs.[87] The structure of $K_{0.36}(H_2O)_yWS_2$ consisted of WS_2 layers and interlayer hydrated K^+, where the WS_2 layers were connected by shared twisted [WS_6] octahedra (Fig. 10i). This electrode exhibited large interlayer spacing of 9.258 Å and high conductivity of 35.8 S m^{-1}. When used as anode for AKIBs, two obvious plateaus at ~−0.15 V in the discharge profile and ~0.05 V in the charge profile were observed, corresponding to the K^+ intercalation/deintercalation process (Fig. 10j). The $K_{0.36}(H_2O)_yWS_2$ obtained a high capacity of 43.3 mA h g^{-1} at 0.2 A g^{-1} within −0.8 to 0.4 V *vs.* Ag/AgCl. The good rate performance of $K_{0.36}(H_2O)_yWS_2$ was ascribed to the high ionic conductivity and large interlayer spacing. Based on *ex situ* XRD results, the highly reversible storage mechanism of hydrated K^+ in $K_{0.36}(H_2O)_yWS_2$ electrode was revealed (Fig. 10k).

Note that metal oxides/sulfides are mainly divided into two categories: intercalation mechanism and conversion mechanism. Most of the intercalated anodes exhibit stable electrochemical performance. However, these materials show low specific capacities and high operating voltages, resulting in low energy densities. For conversion materials, large volume changes caused by conversion reaction will lead to pulverization of the active material, resulting in capacity decay. In addition, large voltage hysteresis and poor first Coulombic efficiency (CE) lead to capacity loss. Therefore, despite the promise of high capacity for this class of materials, these major issues cannot be ignored. Metal oxides/sulfides are still in the primary stages of development as AKIB anode materials, so advanced structural design (nanoengineering or coating) and tuning of electrode/electrolyte interfaces are efficient strategies to achieve highly stable oxides/sulfides anodes.

2.2.3. Alloy. Many elements (such as P, Ge, Sn, Sb, Bi, *etc.*) can undergo alloying reactions with K metal in organic KIBs to achieve efficient K storage.[106–110] These elements have attracted widespread attention for their low operating voltages and high capacities. However, it is rarely reported in AKIBs. Recently, Zheng *et al.* revealed the K^+ storage mechanism of Bi anode in AKIBs.[92] Bi metal exhibited a typical layered structure and possessed a wide interlayer distance of 3.95 Å (Fig. 11a). When used as an AKIB anode, a discharge voltage plateau at ~−0.67 V *vs.* SCE and a charge voltage plateau at ~−0.64 V *vs.* SCE were recorded, indicating the alloying/dealloying reactions with K^+. The Bi anode displayed superior K^+ storage capability, including a high discharge capacity of 181.2 mA h g^{-1} at 0.548 A g^{-1}, a good rate performance, and a long cycle life of over 1600 cycles. Such excellent cyclability was attributed to the highly stable properties of nanorods. Based on *ex situ* XPS characterizations, the process of the alloying reaction (Bi ↔ Bi (K) ↔ BiK_3) was confirmed (Fig. 11b and c). Besides, the full cell consisted of Bi anode and $Co(OH)_2$ cathode was designed. This Bi–Co full cell achieved a high capacity of 157.57 mA h cm^{-2} at 0.5 mA cm^{-2} within a stable operating voltage of 1.6 V. Besides, a high capacity of 127.92 mA h cm^{-2} was maintained after 2500 cycles, demonstrating considerable stability.

In order to deepen the understanding of the energy storage mechanism of Bi anode, Zheng *et al.* carried out a systematic work about Bi storage of different alkali metal ions (Li^+, Na^+, and K^+).[93] The overpotential and voltage polarization in Li^+ electrolyte were the largest, followed by K^+ electrolyte, and the smallest in Na^+ electrolyte. This means that the dealloying reaction of Bi with Li^+ was the most difficult during the entire discharge process, while Na^+ was the easiest. As a result, the Bi anode exhibited the highest capacity and the best rate performance for Na^+ storage, followed by K^+ storage, while it exhibited the lowest capacity and the fastest decay in terms of Li^+ storage (Fig. 11d). Based on the charge density difference, the adsorption energy of Li^+ in Bi layers was highest, manifesting the strongest interaction between Li^+ and Bi (Fig. 11e). In addition,

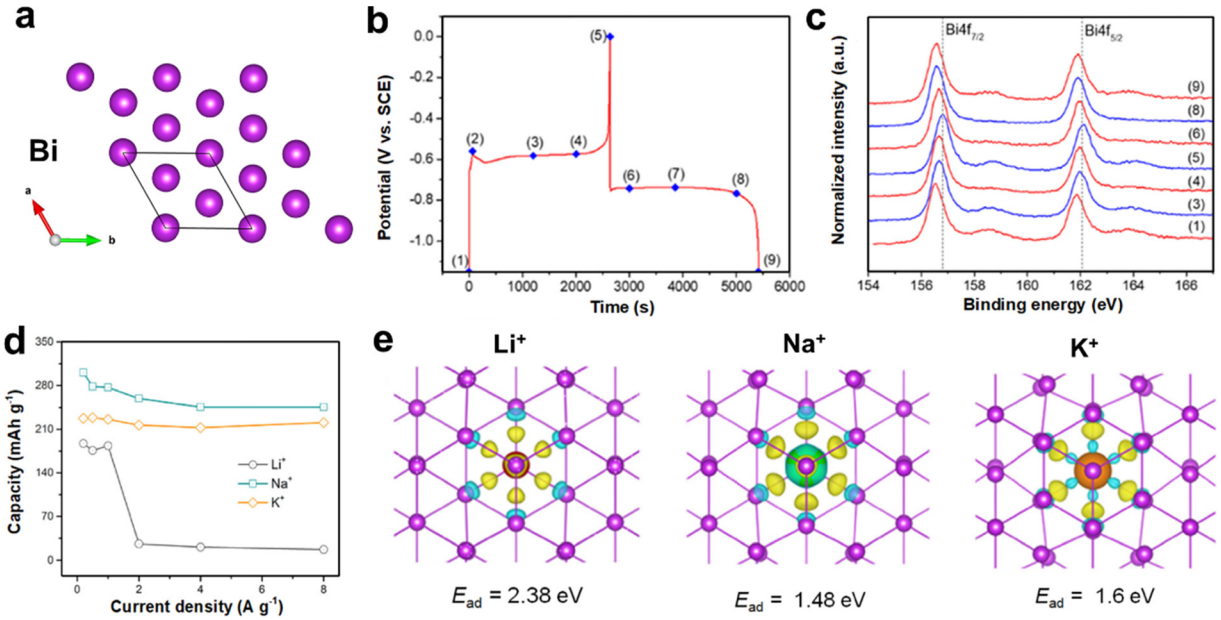

Fig. 11 (a) Crystal structure of Bi. (b) The second GCD profiles of Bi anode at 1 mA cm^{-2}. (c) Corresponding *ex situ* XPS spectrum. Reproduced with permission from ref. 92. Copyright 2020, Elsevier Inc. (d) Rate performance of Bi anode in K^+/Na^+/Li^+ electrolytes. (e) The charge density difference induced by three ions absorption, respectively. Reproduced with permission from ref. 93. Copyright 2022, Elsevier Inc.

8 Li and 8 Na atoms transferred charges to Bi, which were two atoms more than that of K, probably due to the large radius of K^+. Larger volume expansion would cause the capacity of K^+ storage to decline more seriously than that of Na^+ storage.

In summary, alloy material exhibits good electrochemical performance in AKIBs. However, the research on the emerging alloy anode materials for AKIBs is still in its infancy. The main disadvantages of these materials are large volume expansion, various side reactions, and high voltage hysteresis, resulting in poor cycling performance and CEs. With the further development of electrode structure design, as well as in-depth insights into the K^+ storage mechanism and advanced electrolytes, alloy anodes are promising to become one of the stable and high-capacity anodes for AKIBs.

2.2.4. Organic compounds. Unlike the traditional inorganic materials, organic materials show various advantages in the rechargeable battery field, such as diverse chemical structures, good electrochemical stability, low cost, environmental friendliness, and recyclability.[111–116] In general, organic materials show satisfactory specific capacity and rate performance, since large K^+ can be easily de-intercalated into these organic frameworks due to weak intermolecular interactions. Typically, quinones as stable anodes for aqueous batteries were explored by Yao *et al.*[96] The prepared quinones were capable of storing K^+ and other charge-carrying species (such as H^+, Li^+, Na^+, Mg^{2+}) at different pH values, temperatures, and atmospheres. Through the design of quinone molecular structure, three major systems, namely PbO_2 (acidic), $LiMn_2O_4$ (neutral), and $Ni(OH)_2$ (alkaline), were developed. Among these organic molecules, poly(anthraquinonyl sulfide) (PAQS) was especially outstanding as an anode for AKIBs in alkaline electrolytes (pH > 14). PAQS–$Ni(OH)_2$ cell showed a high capacity of 200 mA h g^{-1} in 10 M KOH and good stability of 88% capacity retention after 1350 cycles (Fig. 12a and b). Besides, PAQS exhibited high rate capability at a wide temperature range (25 to −25 °C) due to its lower charge-transfer resistance.

Hu *et al.* proposed 3,4,9,10-perylenetetracarboxylic diimide (PTCDI) as an anode for aqueous K^+ storage.[44] PTCDI anode showed two couples of redox voltage plateaus at −0.45/−0.77 V and −1.05/0.13 V (*vs.* Ag/AgCl) and achieved a discharging capacity of 125 mA h g^{-1} at 0.5C (Fig. 12c). Superior rate performance (110 mA h g^{-1} at 20C) and good cyclability (77% capacity retention over 1000 cycles) were also obtained. The common dissolution of PTCDI anode during the discharge/charge cycle was suppressed when using the concentrated electrolyte. When assembled with the KFeMnHCF cathode, the AKIB full cell possessed a discharge voltage of 1.27 V and remarkable cycling stability. Soon after, Wang *et al.* utilized concentrated electrolyte to suppress the HER of β-perylene-3,4,9,10-tetracarboxylic dianhydride (β-PTCDA) during the discharge/charge process.[94] The redox peaks associated with reversible potassiation/de-potassiation with the carbonyl groups occurred within −1.1 to 0.1 V (*vs.* Hg/Hg_2Cl_2) (Fig. 12d), which may be ascribed to the reversible transition reaction between the C–O–K and C=O bonds. β-PTCDA possessed an initial capacity of 145 mA h g^{-1} at 0.2 A g^{-1} and subsequently a stable capacity of 130 mA h g^{-1}, which were induced by the two-electron reaction from β-PTCDA to K_2PTCDA. Besides, Li and co-workers reported another redox-active polyimide, namely, 1,4,5,8-naphthalenetetracarboxylic dianhydride-derived polyimide (PNTCDA).[95] PNTCDA anode exhibited high reversibility with a discharge capacity of 135 mA h g^{-1} at 2C within −1 to −0.2 V (*vs.* SCE) in KNO_3 electrolyte (Fig. 12e). Compared with the K_2SO_4 electrolyte, PNTCDA showed higher rate performance in the KNO_3 electrolyte.

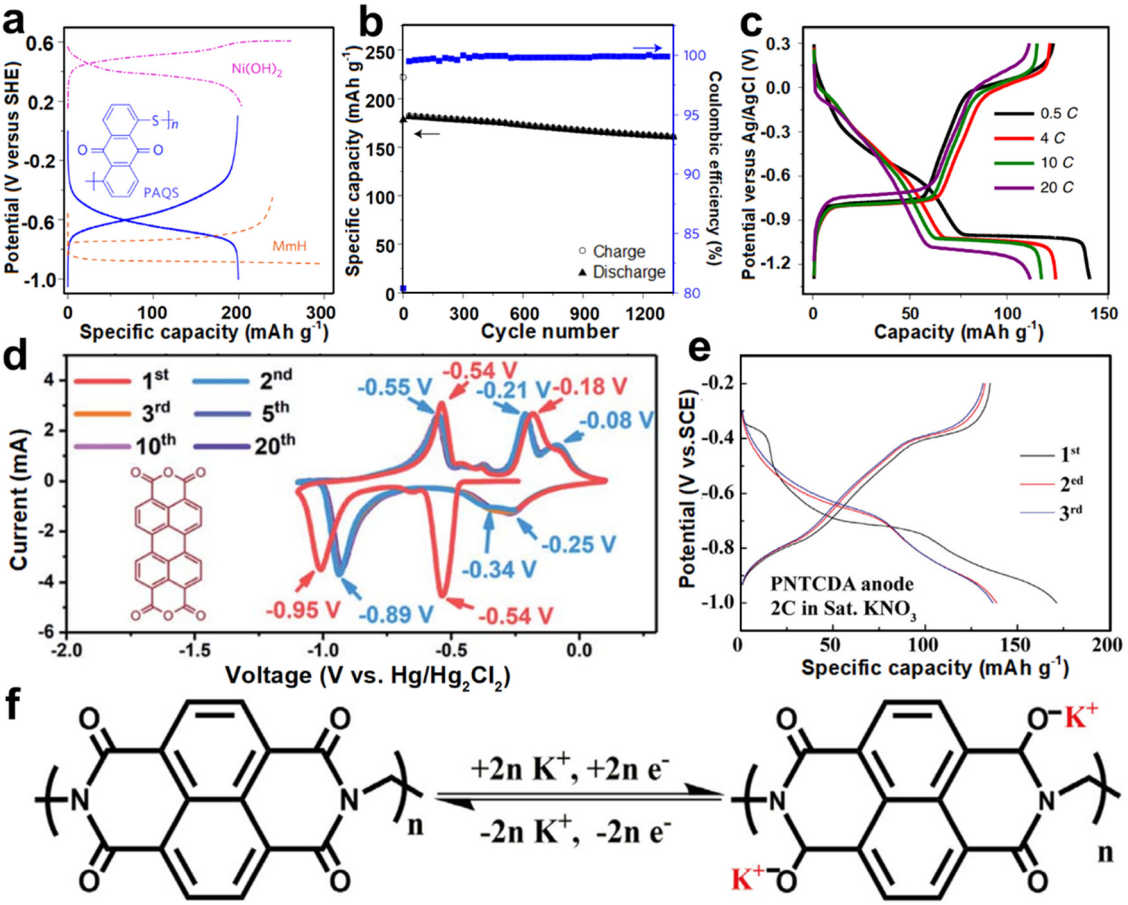

Fig. 12 (a) GCD profiles of PAQS, MmH, and $Ni(OH)_2$. (b) Cycling performance of a PAQS–$Ni(OH)_2$ cell at 1C. Reproduced with permission from ref. 96. Copyright 2017, Springer Nature. (c) GCD profiles of PTCDI at different rates. Reproduced with permission from ref. 44. Copyright 2019, Springer Nature. (d) CV curves of β-PTCDA at 10 mV s^{-1}. Reproduced with permission from ref. 94. Copyright 2020, The Royal Society of Chemistry. (e) GCD profiles of PNTCDA. (f) Schematic illustration of the electrochemical mechanism of PNTCDA. Reproduced with permission from ref. 95. Copyright 2020, Elsevier Inc.

Besides, an enolization process mainly occurred when combined with K^+ insertion/extraction, where charge redistribution in the conjugated structure promoted the reaction (Fig. 12f).

In a word, the main challenge of organic electrode materials is the dissolution in electrolytes. This problem could be greatly reduced with some engineering techniques (high-concentration electrolytes and additives). However, further in-depth research is needed to improve the electronic conductivity and energy density in order to meet the needs of practical applications. One of the common strategies to improve electrical conductivity is to incorporate conductive carbon materials when preparing electrodes, but this method will reduce the tap density of electrodes to a certain extent.

3. Electrolytes for AKIBs

Electrolytes, as ion transport media between cathode and anode, are especially critical in battery systems.[117–123] The liquid electrolyte of AKIBs is to dissolve K salt in water in a certain proportion. The most representative K salts for AKIBs are listed in Table 3 and their physical and chemical properties are summarized. Compared to organic solvents, water is an attractive alternative owing to its fundamental safety, higher ionic conductivity, and low cost.[124] The electrolytes used in AKIBs can be classified into two catalogs, including conventional liquids and hydrogels.

3.1. Aqueous liquid electrolytes

3.1.1. Diluted electrolytes. Water can dissolve most inorganic salts and form solvated structures owing to the coexistence of Lewis basicity of the oxygen position and Lewis acidity of the hydrogen position. According to the Pourbaix plot of water, the stability window shifts to lower voltages as pH increases, allowing more anode material to work in the stable electrolyte window. Generally speaking, the use of dilute K-based electrolytes in AKIBs is as their high ionic conductivity and low cost. The common dilute electrolytes used for AKIBs include 0.5 M K_2SO_4, 1 M KCl, 1 M KNO_3, and 1 M KOH. But the use of dilute electrolytes also faces some obvious problems. For example, hydrolysis inevitably occurs during the charging and discharging processes of the battery, especially under a wide voltage range, causing issues, such as short circuit or even failure of the battery. This is mainly

Table 3 The properties of several common K salts for AKIBs. (The main information of relevant K salts is obtained from Chemiday and Sigma-Aldrich websites)

K Salts	Solubility (g per 100 g H_2O)	Molality (mol kg^{-1})	Ionic Conductivity (maximum value, mS cm^{-1})	Cost ($ per kg)	Toxicity	Ref.
K_2SO_4	12.0	0.7	78.01 (0.48 M)	95.5	Low	125
KCl	35.5	4.8	108.6 (1 M)	132	Nontoxic	125
KNO_3	38.3	3.8	74.28 (0.79 M)	122	Low	125
KOH	121	21.6	626.6 (6 M)	62.1	Moderate	126
KPF_6	9.3	0.5	—	363	Low	89
KFSI	657.7	30	~120 (~5 M)	323 (100 g)	Nontoxic	94
KCF_3SO_3	414.0	22	~140 (~6 M)	104 (25 g)	Nontoxic	44
HCOOK	331 (18 °C)	39.4	130 (10 M)	104	Nontoxic	85
KAc	269	27.4	~112 (~5 M)	330 (2.5 kg)	Low	84

attributed to the existence of abundant water molecules in the dilute electrolyte and the high chemical activity of water. Therefore, it is necessary to develop electrolytes with wide electrochemical windows to improve the electrochemical performance of dilute electrolytes.

3.1.2. Concentrated electrolytes. The narrow electrochemical window (1.23 V) of aqueous electrolytes not only limits the energy density of AKIBs, but also limits the choice of electrodes. Also, the aqueous battery system faced some issues as follows: decomposition of water, side reactions between electrodes and water, co-intercalation of protons, and dissolution of electrodes. In order to solve the above issues to some extent, Wang *et al.* pioneered the proposal of an ultra-concentrated electrolyte (21 M LiTFSI) known as a WiSE electrolyte in 2015.[127] Since then, concentrated electrolytes have been widely used in various aqueous battery systems and shown good electrochemical performance.[128–130] In WiSE electrolytes, the activity of water is suppressed because the content of free water is greatly reduced.

WiSE electrolytes have been successively used in AKIBs, including 22 M KCF_3SO_3, 27.8 M $K(PTFSI)_{0.12}(TFSI)_{0.08}$-$(CF_3SO_3)_{0.8}{\cdot}2H_2O$, 30 M KAc, 30 M KFSI, 40 M HOOCK, and 61.7 M KFSI + KCF_3SO_3.[44,84,85,94,131,132] High concentration electrolytes show several advantages as follows: (1) concentrated electrolytes can widen the ESW. Ji *et al.* first investigated KAc-based WiSE electrolytes in AKIBs, and found that the ESW could be widened to 3.2 V (Fig. 13a).[84] Hu *et al.* reported an AKIB full cell with KCF_3SO_3-based WiSE electrolytes.[44] The 22 M KCF_3SO_3 electrolyte exhibited a wider ESW (3 V, from −1.3 to 1.7 V *vs.* Ag/AgCl), and its redox potential is lower than that in 1 M KCF_3SO_3 electrolyte. Cheng *et al.* proposed 40 M

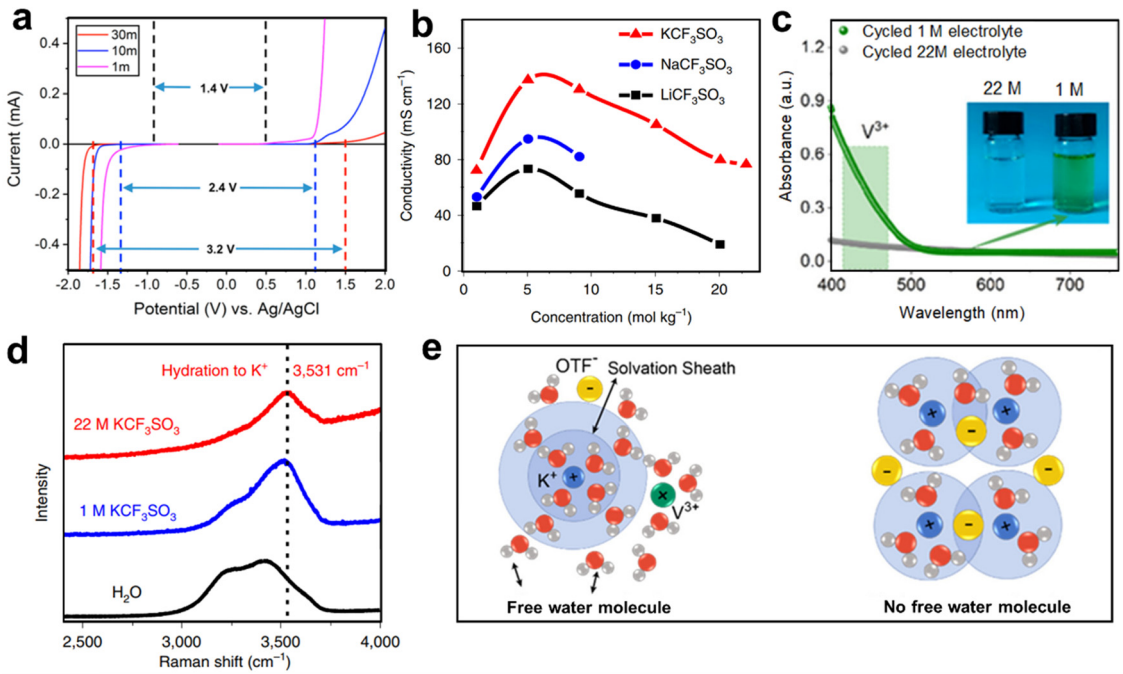

Fig. 13 (a) Linear sweep voltammetry of KAc-based electrolytes. Reproduced with permission from ref. 84. Copyright 2018, American Chemical Society. (b) Ionic conductivity of different concentration $LiCF_3SO_3$-, $NaCF_3SO_3$- and KCF_3SO_3-based electrolytes. Reproduced with permission from ref. 44. Copyright 2019, Springer Nature. (c) UV-vis spectroscopy of the cycled 1 and 22 M KCF_3SO_3-based electrolytes. Reproduced with permission from ref. 54. Copyright 2021, American Chemical Society. (d) The Raman spectrum of two electrolytes and H_2O. Reproduced with permission from ref. 44. Copyright 2019, Springer Nature. (e) Schematic illustration of the solvation structure in two electrolytes. Reproduced with permission from ref. 54. Copyright 2021, American Chemical Society.

HCOOK-based WiSE electrolytes, showing a wide ESW up to 4 V.[85] Wang *et al.* explored 30 M KFSI-based WiSE electrolyte with the ESW of 3.97 V.[94] (2) Concentrated electrolytes can improve the electronic conductivity. At the same concentration, the conductivity of KAc-based electrolytes is higher than that of other reported fluorinated imide salts such as LiTFSI.[84] The higher conductivity may be ascribed to the dominance of acetate salt or the Lewis weak acidity of K^+. Compared with $LiCF_3SO_3$ and $NaCF_3SO_3$, the high concentration of KCF_3SO_3 exhibited a series of excellent properties, high ionic conductivity (76 mS cm^{-1} at room temperature), low viscosity, and wide voltage window (Fig. 13b).[44] The conductivity of HOOCK-based electrolyte reached about 130 mS cm^{-1} at 10 M and still maintained 46 mS cm^{-1} even at 40 M, which exceeded other fluorinated imine-based WiSE electrolytes and previously reported KAc.[85] The electrical conductivity of KFSI-based electrolytes also surpasses those of LiTFSI-based electrolytes and KAc-based electrolytes at the same concentrations.[94] (3) Concentrated electrolytes can effectively prohibit the dissolution of electrode. UV-vis spectra showed the existence of strong adsorption of V^{3+} ions in the cycled 1 M KCF_3SO_3-based electrolyte, while no adsorption occurred in the 22 M KCF_3SO_3-based electrolyte, indicating that the high concentration electrolyte inhibited the dissolution of the δ-$K_{0.5}V_2O_5$ (Fig. 13c).[54] Similarly, the electrolyte turned pink after 5 cycles for PTCDI anode in 1 M KCF_3SO_3 electrolyte, while it was still transparent in 22 M KCF_3SO_3 electrolyte, indicating that the dissolution in the concentrated electrolyte was effectively suppressed.[44] A similar phenomenon was also observed in 30 M KFSI-based electrolyte, which ensured the integrity of β-PTCDA and achieved long-term cycling performance.[94]

It is worth mentioning that the widened voltage window and suppressed dissolution properties are associated with the reduction of free water in concentrated electrolytes. As shown in Fig. 13d, the water state in 1 M electrolyte was similar to that of pure water, indicating that a large amount of free molecular water existed in the electrolyte with low concentration, so that the V^{3+} species could be dissolved in the electrolyte.[44] In the 22 M electrolyte, weak hydrogen bonds remained and shifted to the right, while strong hydrogen bonds gradually disappeared, indicating that the strong K^+ solvation effect confines water molecules. The confined free water in WiSE only dissolved the limited V^{3+}, which hindered the dissolution of the active electrode (Fig. 13e).[54]

3.1.3. Electrolyte additives. Although substantial progress in the area of AKIBs with concentrated electrolytes has been achieved, they still suffer from the high cost, which hinders the large-scale application of aqueous energy storage devices. Clearly, the use of electrolyte additives is considered to be another economical and efficient way to solve the main problems of AKIB electrolytes. In fact, electrolyte additives have been widely used in aqueous and organic batteries to stabilize the electrode/electrolyte interface, suppress the growth of metal anode dendrites, improve extreme environmental adaptability, and increase the flame retardancy of electrolytes, *etc.*[133–141] The reported additives for aqueous battery electrolytes are mainly divided into four types, including ionic additives, organic additives, inorganic additives, and metal additives.[134] Ionic additives mainly adjust the electrochemical stability of electrolytes by introducing ions to change the ionic charge size, bond energy, solvation structure, interfacial electric double layer structure, *etc.* in the electrolytes.[142,143] Organic additives, including small molecules, organic acids, surfactants, and polymers, mainly affect the performance of anodes.[144,145] For example, surfactant-based additives tend to adsorb on the interface between the electrolyte and electrode, and optimize the performance of the anodes by affecting the interface contact energy barrier, the desolvation process, and the deposition process of alkali metal ions. In addition, inorganic and metal additives are mainly utilized to modify the surface texture of alkali metals for the deposition control of anodes, and the effective inhibition of dendrite growth is due to their limited low solubility.[146,147]

Sugar, as an organic additive, can decrease the content of free water and change the tetrahedral structure of water. Xue *et al.* explored inexpensive, readily available sugar-concentrated aqueous electrolytes for AKIBs.[31] The amount of free water molecules decreased with the increase of sugar concentration. The tetrahedral structure of water was destroyed by the super-concentrated sugar, which broke the hydrogen bonds to reduce the binding degree of water molecules. These sugar-based electrolytes exhibited a wide ESW of ~2.812 V, wide operating temperature range, and good ionic conductivity. Ultra-concentrated maltose significantly improved the first discharge capacity, which was increased from 29.2 mA h^{-1} to 69.6 mA h^{-1} after adding super-concentrated maltose (Fig. 14a and b). Besides, the capacity retention over 2000 cycles in 1 M KNO_3/60.0 wt% maltose electrolyte was higher than that of in 1 M KNO_3 electrolyte.

DMF, as another organic additive, can promote the anions decomposition and promote the formation of robust solid electrolyte interfaces (SEI). A 2 M KFSI diluted electrolyte using a mixed solvent of *N*,*N*-dimethylformamide/water (DMF/H_2O) was developed by Li *et al.*[86] The addition of DMF enabled the electrolyte with a window of 2.89 V, which is wider than the bare water electrolyte (2.66 V), along with low viscosity, high conductivity, and high safety (Fig. 14c). Also, DMF solvent showed a lower LUMO energy than that of H_2O solvent, which could facilitate the decomposition of FSI^- to form $-CF_x$ and KF, generating a robust solid electrolyte interphase (Fig. 14d).

$Zn(CF_3SO_3)_2$, as an ionic additive, can change the K^+ storage mechanism of electrode materials through the liquid phase. Mai *et al.* found different electrochemical energy storage mechanisms of $K_{2.55}Zn_{3.08}[Fe(CN)_6]_2{\cdot}0.28H_2O$ (KZnHCF) electrode material in different electrolytes.[48] Both solid solution and two-phase mechanisms were found in 0.5 M K_2SO_4 and 1.0 M KCF_3SO_3 electrolytes, while only the solid solution mechanism was found in 5.0 M KCF_3SO_3 and 3.0 M KCF_3SO_3 + 2.0 M $Zn(CF_3SO_3)_2$ electrolytes (Fig. 14e). Zn^{2+} acted as a replacement for K^+ in the electrolyte, resulting in the significantly enhanced structural stability of KZnHCF during K^+ insertion/extraction. This liquid-phase-induced solid-solution-phase ion storage mechanism enabled stable cycling of the KZnHCF electrode material for 10 000 cycles.

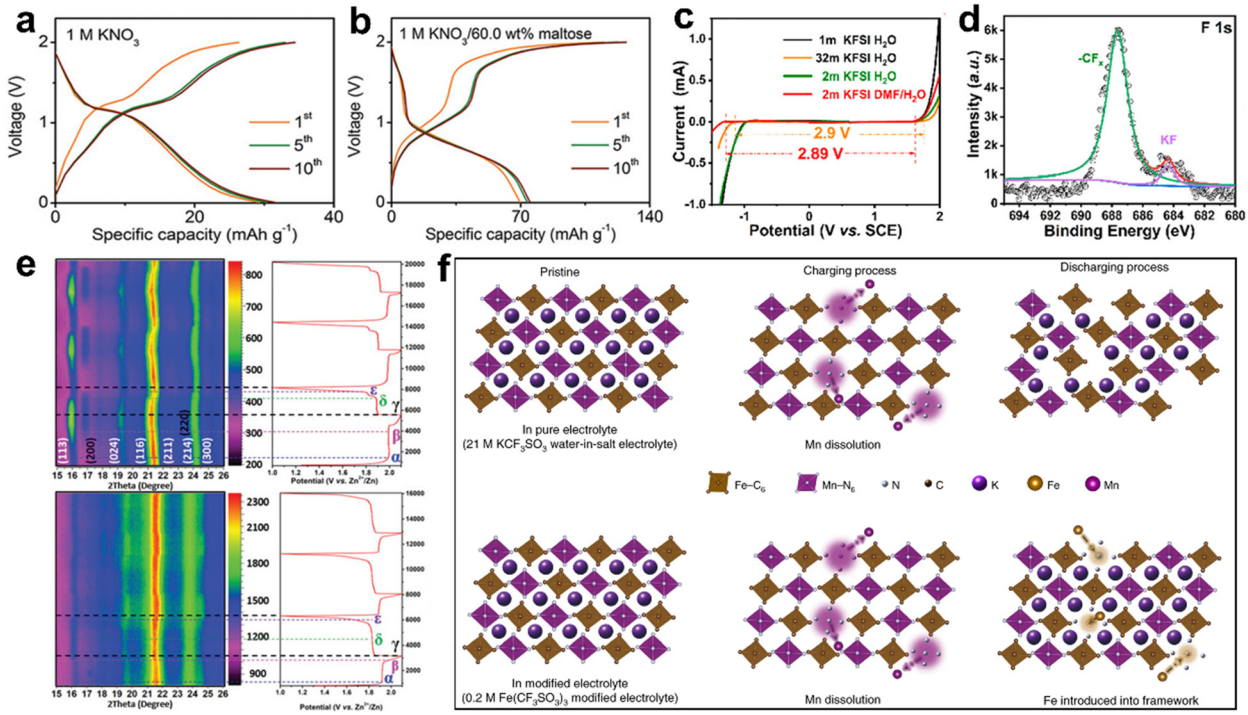

Fig. 14 GCD profiles of PB-K//AC battery in (a) KNO_3 electrolyte and (b) KNO_3/60.0 wt% maltose electrolyte. Reproduced with permission from ref. 31. Copyright 2020, Wiley-VCH. (c) ESW of KFSI in aqueous electrolytes with and without DMF. (d) *Ex situ* XPS spectrum of F1s in 2 M KFSI DMF/H_2O electrolyte. Reproduced with permission from ref. 86. Copyright 2021, American Chemical Society. (e) *In situ* XRD patterns and the corresponding GCD profiles in 1.0 M KCF_3SO_3 and 3.0 M KCF_3SO_3 + 2.0 M $Zn(CF_3SO_3)_2$ electrolytes. Reproduced with permission from ref. 48. Copyright 2021, Wiley-VCH. (f) Schematic illustration of the electrochemical behavior of KMnF electrode in 21 M KCF_3SO_3 aqueous electrolyte with and without $Fe(CF_3SO_3)_3$. Reproduced with permission from ref. 46. Copyright 2021, Springer Nature.

$Fe(CF_3SO_3)_2$, as another ionic additive, can inhibit the dissolution of the material by surface modification. Lu *et al.* developed an *in situ* electrochemical cation substitution method by adding a certain amount of iron ions (Fe^{3+}) into the electrolyte.[46] The surface of $K_{1.82}Mn[Fe(CN)_6]_{0.96}\cdot 0.47H_2O$ (KMnF) was modified and converted into a $KFe_xMn_{1-x}F$ electrode by the electrolyte (Fig. 14f). Although the initial dissolution of manganese was not suppressed, the introduced Fe^{3+} filled the vacancies generated by the manganese dissolution during the discharge process, so that the entire framework of the PB material was stabilized. The substitution reaction occurred on the electrode surface, so that a film was formed, which could inhibit the further dissolution of Mn and absorption of Fe.

3.2. Hydrogel electrolytes

Liquid electrolytes are common in aqueous energy storage devices due to their high ionic conductivity. However, liquid electrolyte devices may suffer from electrolyte leakage and unsatisfactory dislocations when stressed. To avoid these issues, hydrogel electrolytes are introduced, *i.e.*, some hydrophilic polymers can be introduced into the K salt aqueous solution. Hydrogel electrolytes exhibit high physical flexibility and good electrochemical performance.[148–152]

Polyvinyl alcohol (PVA) and carboxymethyl cellulose sodium (CMC) based hydrogel has been used in AKIBs. Ma *et al.* assembled a flexible solid-state symmetric AKIB with PB electrode and KCl-PVA hydrogel electrolyte (Fig. 15a).[32] It is worth noting that an ESW of ~1.3 V and an ionic conductivity of 3.7×10^{-2} S cm^{-1} could be achieved using PVA-based hydrogel electrolyte, which provided satisfactory feasibility to fabricate flexible batteries. The flexible full cell exhibited an average potential of ~0.6 V with a high capacity of 58 mA h g^{-1} at 100 mA g^{-1} (Fig. 15b). An outstanding capacity retention of 98.5% at the bending angle of 60° was delivered. However, the following capacity decayed during the cycle test may be caused by the evaporation of water that reduces the ionic conductivity and increases the interfacial overpotential. Soon after, Jiang *et al.* assembled an all-solid-state flexible AKMB on a poly(methyl methacrylate) (PMMA) substrate using KCl-PVA hydrogel electrolyte to meet the specific micropower requirements of wearable electronic devices (Fig. 15c).[90] The all-solid-state AKMB exhibited almost no capacity fading when bent to 90° due to its outstanding mechanical flexibility (Fig. 15d). In addition, AKIB was assembled with thin-film solar cells into a self-powered system, powering the LED lights when sunlight was available, showing potential applications in electronic microdevices (Fig. 15e).

Recently, Varzi *et al.* developed another hydrogel electrolyte by adding CMC to a highly concentrated aqueous electrolyte.[47] The instability issue of KMHCF in the alkaline environment caused by the acetate-based electrolyte was solved. Molecular dynamics simulation calculations showed that the presence of CMC lowered the movement of water molecules and acetate ions by ~2 times, while the movement of K^+ was 2.2 times faster when the electrolyte viscosity increased (Fig. 15f). The

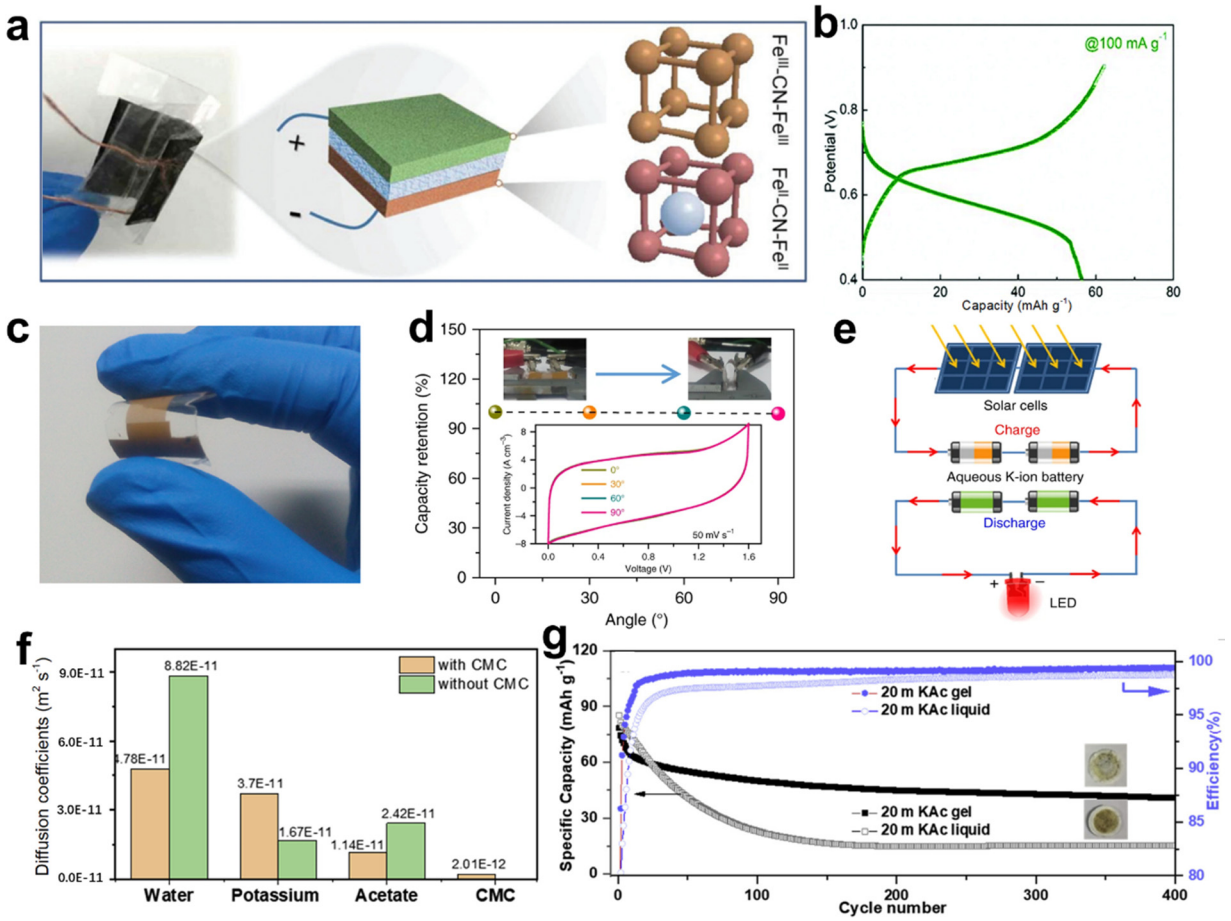

Fig. 15 (a) Schematic illustration of symmetric AKIB with KPB bipolar electrodes and PVA hydrogel electrolyte. (b) GCD profiles of a full cell at 100 mA g^{-1}. Reproduced with permission from ref. 32. Copyright 2018, The Royal Society of Chemistry. (c) Photograph of flexible AKMBs with PVA hydrogel electrolyte. (d) Capacity retention of flexible AKMBs under different bending angles. (e) Schematic illustration of a self-powered system assembled with flexible AKMBs and thin-film solar cells. Reproduced with permission from ref. 90. Copyright 2019, Springer Nature. (f) Diffusion coefficient of electrolyte component with and without CMC. (g) Cycling performance of KMHCF with the liquid and gel electrolytes. Reproduced with permission from ref. 47. Copyright 2020, Elsevier Inc.

hydrogel electrolyte possessed a high ionic conductivity of 22.3 mS cm^{-1} and a wide ESW. As a result, KMHCF with gel electrolyte showed better cyclability and higher CEs than liquid electrolyte due to the reduced Fe and Mn dissolution (Fig. 15g).

In conclusion, the electrochemical performance of a battery is closely associated with electrolytes. In different electrolyte systems, electrode materials exhibit completely different electrochemical behaviors. Despite these advances, hydrogel electrolytes still lack some properties suitable for commercial applications, such as lower ionic conductivity, poor electrode/electrolyte interface, and higher overpotentials compared with liquid electrolytes. Therefore, further research is needed in the field of electrolytes to match the cathode and anode to make this potential system useful for practical applications.

4. Full cells for AKIBs

The significant challenges that AKIB still faces are not limited to improving the operating voltage and capacity of half-cells. More importantly, the cathode and anode materials can be combined to work together to ensure that the full cells meet the energy density requirements. Ensuring the economic sustainability of AKIB full cells has significant implications for large-scale energy storage needs. AKIB full cells consist of cathodes, anodes, separators, and electrolytes, and these components can be used to design full-cells in different configurations as needed. In the laboratory, components for full-cell designs are typically assembled in coin cell-type devices (CR2016, CR2025, or CR2032). Currently commonly used cathode materials for AKIB full cells include PBA, layered vanadium oxide, and hydroxide. The anode materials matched with them include organics, $KTi_2(PO_4)_3$, alloy materials, and Zn flakes. It is worth noting most of the cathodes and anodes of full cells usually require an activation process, *i.e.*, pre-potassiation, in the half-cell to eliminate the detrimental effects during initial cycling. In addition, before full-cell assembly, it is often necessary to control the mass ratio of anode and cathode to optimize their charge balance.

Fig. 16 shows the electrochemical performance of representative AKIB full cells. PBAs and organic materials were the most frequently used cathode and anode materials, respectively. KZnHCF//Zn and KMnF//PTCDI exhibited the highest voltage

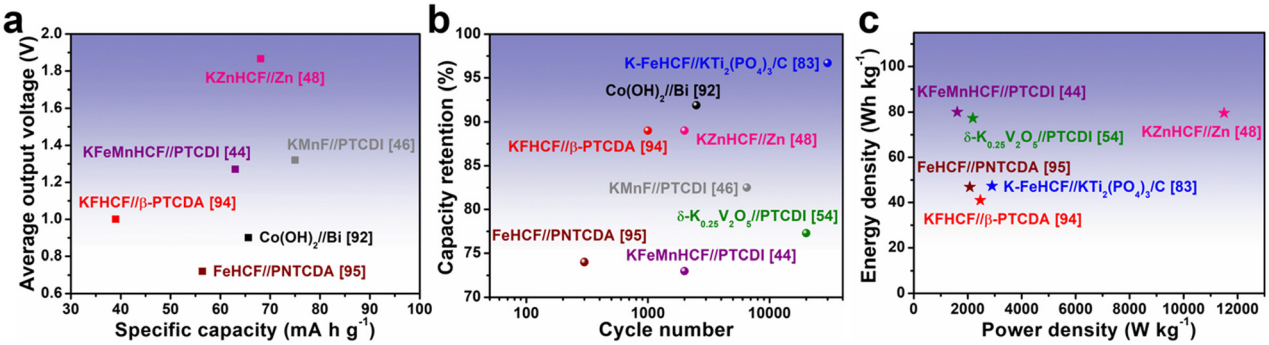

Fig. 16 (a) Average output voltage *versus* specific capacity, (b) capacity retention *versus* cycle number, and (c) energy density *versus* power density of selected AKIB full cells reported in the literature.

output (~1.87 V) and the highest specific capacity (75 mA h g^{-1}), respectively, however, these two satisfactory combinations still need further improvement (Fig. 16a).[46,48] As shown in Fig. 16b, some systems, such as K-FeHCF//$KTi_2(PO_4)_3$/C and δ-$K_{0.25}V_2O_5$//PTCDI, still displayed considerable capacity retention even after tens of thousands of cycles.[54,83] The energy densities of most systems were less than 100 W h kg^{-1}, indicating that the cyclability and power output may be sufficient, while the energy densities were still lower than aqueous batteries using other metal carriers (Fig. 16c). It is noteworthy that most AKIB full-cell systems (K-FeHCF//$KTi_2(PO_4)_3$/C, KFHCF//β-PTCDA, δ-$K_{0.5}V_2O_5$//PTCDI, and KFeMnHCF//PTCDI) were assembled based on high-concentration electrolytes, which would increase the cost and reduce the energy density of the battery.[44,54,83,94] In addition, pouch cells (KFeMnHCF//PTCDI, KMnF//PTCDI, and δ-$K_{0.25}V_2O_5$//PTCDI) exhibited excellent wide temperature performance, showing application potential under extreme conditions.[44,46,54]

To sum up, the operating voltage, cycle performance, and cost of the cathode are the bottlenecks restricting its further practical application. The electrochemical behavior of cathodes and anodes of AKIBs, such as capacity utilization, balance, and electrolyte compatibility, requires in-depth study. In particular, electrolyte compatibility between electrode and electrolyte or between cathode and anode electrodes is an important factor.

5. Summary and perspectives

AKIBs have received increasing attention in the field of large-scale ESSs thanks to their low price, high power density, environmental friendliness, and high safety. This review systematically overviewed the recent advances in AKIB research and discussed strategies for improving electrochemical performance, including cathodes, electrolytes, and anodes. Although some remarkable advances have been achieved in AKIBs, further research is needed to fulfill the requirements of practical applications of high-performance AKIBs. This section will evaluate the current key electrode materials, characterization techniques, theoretical calculations, and applications (Fig. 17).

5.1 Key materials

Designing high-performance electrode materials for AKIBs is more challenging than ALIBs and ASIBs, because K^+ is much larger than Na^+ and Li^+. Current cathode materials for AKIBs still exhibit limited weight/volume energy capacity. PB and PBAs show superior cycling stability and high voltage platform, which are common cathode materials for AKIBs. However, the capacities of PB and PBAs need to be further boosted before successful commercialization. Vanadium-based oxides are important electrodes due to their reversibility, but the output voltage is slightly inferior to PB. Polyanionic compounds and MXenes as K^+ storage cathode materials exhibit high working voltage, but low capacity.

For the anode materials for AKIBs, the current research is still mainly focused on organic materials and polyanionic compounds, and attempts to use metal compounds/sulfides and alloy-based materials, *etc.* Although the developed organic electrode materials exhibit excellent K^+ storage ability, most of them benefit from the concentrated electrolytes, and the issue of easy dissolution requires extra strategies to improve. NASICON-type $KTi_2(PO_4)_3$ shows relatively low potential but good cycling stability, and their low capacity limits their practical applications. Despite the high capacity and energy density of metal oxide/sulfide and alloyed anodes, the active

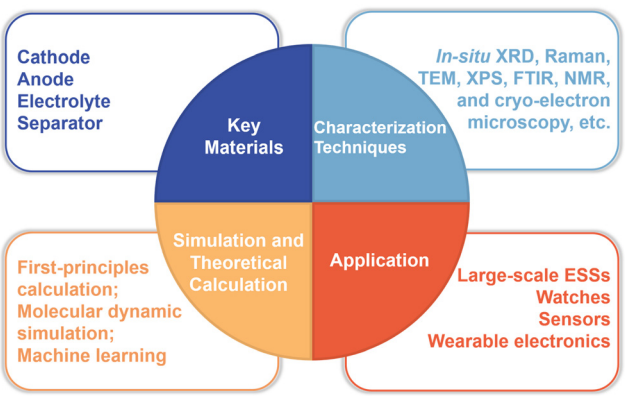

Fig. 17 The opportunities and future directions for achieving high-performance AKIBs.

anode particles experience large volume changes, resulting in poor cycling stability with further pulverization and aggregation. Thus, to facilitate the commercial viability of AKIBs by matching with cathode materials, fundamental breakthroughs of anode materials with high performance must be achieved.

The current situation is that the choice of cathode and anode materials is limited. Strategies adopted to modify the electrochemical properties of cathode and anode materials for AKIBs are far from adequate compared to the organic systems. Generally speaking, the ideal electrode material needs to meet the following requirements: (1) suitable redox potential (high redox potential for the cathode, low redox potential for the anode), (2) high specific K^+ storage capacity, (3) good compatibility with electrolyte, (4) high electronic and ionic conductivity, (5) excellent structural stability, (6), high thermal and chemical stability, (7) environmentally friendly, and (8) low cost. To realize high-performance AKIBs, it is urgently needed to continuously discover and develop novel cathode and anode materials with the above properties. More strategies to improve the electrochemical performance of AKIB electrode materials are needed, including composites with highly conductive materials, morphology design, surface modification, element doping, and electrolyte optimization.

AKIB electrolytes, especially the traditional liquid electrolytes, have taken a leap forward in recent years. One type of aqueous electrolytes is the diluted electrolyte, which can be easily prepared by using K_2SO_4, KCl, KNO_3, and KOH salts. In recent years, other concentrated aqueous electrolytes based on KAc, KCF_3SO_3, HOOCK, and KFSI have been developed, and the voltage range could be greatly extended to 3–4 V, which is a significant research direction for AKIBs. In addition, a certain amount of additives in the electrolyte could stabilize the electrode material by utilizing the common ion effect. Hydrogel electrolytes are obtained by adding polymers such as PVA and CMC to the conventional aqueous electrolytes, which may advance the application of flexible K^+ storage devices. In general, an ideal electrolyte should demonstrate the following major properties: (1) high ionic conductivity for fast K^+ transport, (2) stable and wide electrochemical window with no parasitic side reactions (HER, OER, or electrode dissolution, *etc.*), (3) good wettability, (4) excellent wide temperature application capability, (5) environmental friendliness, and (6) low cost. In order to achieve the above goals of high-performance electrolytes, strategies such as adding additives, adjusting concentrations, and using gel electrolytes may be expected to be realized. In addition, the investigation on AKIB separators is lacking.

5.2 Advanced characterization techniques

During the electrochemical process of an alkali metal ion battery, all components (cathode, anode, and electrolyte) are relatively dynamic. The electrochemical stability of the battery is closely associated with these changes in the internal structure or composition. Therefore, there is an increasing need to apply *in situ* characterization techniques to collect electrochemical information in real time, especially for those transient processes that generate unstable phases. *In situ* characterization has been widely used in LIB research, but its application in AKIB research is still lacking. Advanced *in situ* characterization techniques (such as XRD, XPS, cryo-electron microscopy, TEM, STEM, Raman spectroscopy, and Fourier transform infrared microscopy) can help analyze the K^+ insertion/extraction process, interfacial reaction, the transport of K^+ ions, and gain more details about the side reactions. In addition, the combined technology of *in situ* characterization system is the trend of future development, such as spectroscopy-electrical *in situ* characterization system.

5.3 Theoretical calculations

Combined with advanced characterization techniques, theoretical calculations, and machine learning can be used as auxiliary tools to deepen the basic understanding of the AKIB mechanism. For example, molecular dynamic simulations and first-principles calculations can provide detailed information on the behavior of redox reactions at the molecular and atomic levels, respectively. Moreover, according to DFT calculations, the adsorption energies of intermediates can be calculated and analyzed to reveal the preferred reaction paths of electrodes in specific electrolytes. In addition, artificial intelligence and machine learning will play an equally important role in predicting and optimizing the most reasonable material combination and battery design.

5.4 Applications

AKIBs are expected to be applied to large-scale ESSs in the future, including tiny electronic devices, sensor devices, and flexible wearable electronic devices. The industrialization of AKIBs will comprehensively consider these key components, including cathode, anode, electrolyte, separator, current collector, battery packaging and manufacturing, cost, and performance. Furthermore, when a relatively expensive and high-concentration electrolyte is applied to AKIBs, its cost should be evaluated. Overall, a timely assessment of the existing problems and solutions in AKIBs will facilitate the translation of laboratory-based research battery designs into the industry.

Conflicts of interest

There are no conflicts to declare.

Acknowledgements

This work was supported by the National Natural Science Foundation of China (51832004, 21905218), the Key Research and Development Program of Hubei Province (2021BAA070), the Natural Science Foundation of Hubei Province (2019CFA001, 2020CFB519), the Sanya Science and Education Innovation Park of Wuhan University of Technology (2021KF0019, 2020KF0019), and the Fundamental Research Funds for the Central Universities (WUT: 2020IVB034, 2020IVA036). This work was supported by the Singapore Ministry of Education Academic Research Fund Tier 2 (MOE2019-T2-2-127 and MOE-T2EP50120-0002), A*STAR

under AME IRG (A2083c0062), and the Singapore National Research Foundation Competitive Research Program (NRF-CRP18-2017-02). This work was supported by A*STAR under its IAF-ICP Programme I2001E0067 and the Schaeffler Hub for Advanced Research at NTU. This work was also supported by NTU-PSL Joint Lab collaboration. X. Z. gratefully acknowledges financial support from the Chinese Scholarship Council.

References

1 D. Larcher and J.-M. Tarascon, *Nat. Chem.*, 2015, **7**, 19–29.
2 Z. Yang, J. Zhang, M. C. W. Kintner-Meyer, X. Lu, D. Choi, J. P. Lemmon and J. Liu, *Chem. Rev.*, 2011, **111**, 3577–3613.
3 O. Schmidt, A. Hawkes, A. Gambhir and I. Staffell, *Nat. Energy*, 2017, **2**, 1–8.
4 D. Chao, W. Zhou, F. Xie, C. Ye, H. Li, M. Jaroniec and S.-Z. Qiao, *Sci. Adv.*, 2020, **6**, eaba4098.
5 J. M. Tarascon and M. Armand, *Materials for sustainable energy: a collection of peer-reviewed research and review articles from Nature Publishing Group*, World Scientific, 2011, pp. 171–179.
6 N. Nitta, F. Wu, J. T. Lee and G. Yushin, *Mater. Today*, 2015, **18**, 252–264.
7 K. Liu, Y. Liu, D. Lin, A. Pei and Y. Cui, *Sci. Adv.*, 2018, **4**, eaas9820.
8 W. Li, J. R. Dahn and D. S. Wainwright, *Science*, 1994, **264**, 1115–1118.
9 Z. Li, D. Young, K. Xiang, W. C. Carter and Y. M. Chiang, *Adv. Energy Mater.*, 2013, **3**, 290–294.
10 V. D. Neff, *J. Electrochem. Soc.*, 1978, **125**, 886.
11 C. Xu, B. Li, H. Du and F. Kang, *Angew. Chem., Int. Ed.*, 2012, **124**, 957–959.
12 R. Y. Wang, C. D. Wessells, R. A. Huggins and Y. Cui, *Nano Lett.*, 2013, **13**, 5748–5752.
13 S. Liu, J. J. Hu, N. F. Yan, G. L. Pan, G. R. Li and X. P. Gao, *Energy Environ. Sci.*, 2012, **5**, 9743–9746.
14 H. Zhang, X. Tan, H. Li, S. Passerini and W. Huang, *Energy Environ. Sci.*, 2021, **14**, 5788–5800.
15 M. Li, Z. Li, X. Wang, J. Meng, X. Liu, B. Wu, C. Han and L. Mai, *Energy Environ. Sci.*, 2021, **14**, 3796–3839.
16 H. Kim, J. Hong, K.-Y. Park, H. Kim, S.-W. Kim and K. Kang, *Chem. Rev.*, 2014, **114**, 11788–11827.
17 S. Gheytani, Y. Liang, F. Wu, Y. Jing, H. Dong, K. K. Rao, X. Chi, F. Fang and Y. Yao, *Adv. Sci.*, 2017, **4**, 1700465.
18 X. Tang, D. Zhou, B. Zhang, S. Wang, P. Li, H. Liu, X. Guo, P. Jaumaux, X. Gao, Y. Fu, C. Wang, C. Wang and G. Wang, *Nat. Commun.*, 2021, **12**, 2857.
19 F. Wang, X. Fan, T. Gao, W. Sun, Z. Ma, C. Yang, F. Han, K. Xu and C. Wang, *ACS Cent. Sci.*, 2017, **3**, 1121–1128.
20 X. Sun, V. Duffort, B. L. Mehdi, N. D. Browning and L. F. Nazar, *Chem. Mater.*, 2016, **28**, 534–542.
21 X. Wu, Y. Qi, J. J. Hong, Z. Li, A. S. Hernandez and X. Ji, *Angew. Chem., Int. Ed.*, 2017, **56**, 13026–13030.
22 W. Zhang, Y. Liu and Z. Guo, *Sci. Adv.*, 2019, **5**, eaav7412.
23 G. Liang, F. Mo, X. Ji and C. Zhi, *Nat. Rev. Mater.*, 2021, **6**, 109–123.
24 B. Tang, L. Shan, S. Liang and J. Zhou, *Energy Environ. Sci.*, 2019, **12**, 3288–3304.
25 L. Xia, L. Yu, D. Hu and G. Z. Chen, *Mater. Chem. Front.*, 2017, **1**, 584–618.
26 M. R. Lukatskaya, B. Dunn and Y. Gogotsi, *Nat. Commun.*, 2016, **7**, 1–13.
27 M. Huang, M. Li, C. Niu, Q. Li and L. Mai, *Adv. Funct. Mater.*, 2019, **29**, 1807847.
28 M. Song, H. Tan, D. Chao and H. J. Fan, *Adv. Funct. Mater.*, 2018, **28**, 1802564.
29 M. Xia, X. Zhang, T. Liu, H. Yu, S. Chen, N. Peng, R. Zheng, J. Zhang and J. Shu, *Chem. Eng. J.*, 2020, **394**, 124923.
30 L. C. Lopes, S. Husmann and A. J. G. Zarbin, *Electrochim. Acta*, 2020, **345**, 136199.
31 H. Bi, X. Wang, H. Liu, Y. He, W. Wang, W. Deng, X. Ma, Y. Wang, W. Rao and Y. Chai, *Adv. Mater.*, 2020, **32**, 2000074.
32 K. Lu, H. Zhang, S. Gao, Y. Cheng and H. Ma, *Nanoscale*, 2018, **10**, 20754–20760.
33 K. Itaya, T. Ataka and S. Toshima, *J. Am. Chem. Soc.*, 1982, **104**, 4767–4772.
34 K. Honda and H. Hayashi, *J. Electrochem. Soc.*, 1987, **134**, 1330.
35 C. D. Wessells, R. A. Huggins and Y. Cui, *Nat. Commun.*, 2011, **2**, 1–5.
36 C. D. Wessells, S. V. Peddada, R. A. Huggins and Y. Cui, *Nano Lett.*, 2011, **11**, 5421–5425.
37 C. D. Wessells, M. T. McDowell, S. V. Peddada, M. Pasta, R. A. Huggins and Y. Cui, *ACS Nano*, 2012, **6**, 1688–1694.
38 X. Wei, J. Wei, Y. Song, D. Wu, X. D. Liu, H. Chen, P. Xiao and Y. Zhang, *Chem. Commun.*, 2021, **57**, 7019–7022.
39 D. Su, A. McDonagh, S. Z. Qiao and G. Wang, *Adv. Mater.*, 2017, **29**, 1604007.
40 L. Zhang, L. Chen, X. Zhou and Z. Liu, *Adv. Energy Mater.*, 2015, **5**, 1400930.
41 M. Huang, X. Wang, J. Meng, X. Liu, X. Yao, Z. Liu and L. Mai, *Nano Energy*, 2020, **77**, 105069.
42 C. Li, X. Wang, W. Deng, C. Liu, J. Chen, R. Li and M. Xue, *ChemElectroChem*, 2018, **5**, 3887–3892.
43 W. Ren, X. Chen and C. Zhao, *Adv. Energy Mater.*, 2018, **8**, 1801413.
44 L. Jiang, Y. Lu, C. Zhao, L. Liu, J. Zhang, Q. Zhang, X. Shen, J. Zhao, X. Yu and H. Li, *Nat. Energy*, 2019, **4**, 495–503.
45 K. Zhu, Z. Li, T. Jin and L. Jiao, *J. Mater. Chem. A*, 2020, **8**, 21103–21109.
46 J. Ge, L. Fan, A. M. Rao, J. Zhou and B. Lu, *Nat. Sustain.*, 2021, 1–10.
47 J. Han, A. Mariani, H. Zhang, M. Zarrabeitia, X. Gao, D. V. Carvalho, A. Varzi and S. Passerini, *Energy Storage Mater.*, 2020, **30**, 196–205.
48 M. Huang, J. Zhu, R. Yu, Y. Liu, X. Liu, J. Wu, Q. An and L. Mai, *Adv. Energy Mater.*, 2021, **11**, 2102342.
49 P. Padigi, J. Thiebes, M. Swan, G. Goncher, D. Evans and R. Solanki, *Electrochim. Acta*, 2015, **166**, 32–39.
50 A. Baioun, H. Kellawi and A. Falah, *Curr. Nanosci.*, 2018, **14**, 227–233.

51 W. Song, X. Ji, Y. Zhu, H. Zhu, F. Li, J. Chen, F. Lu, Y. Yao and C. E. Banks, *ChemElectroChem*, 2014, **1**, 871–876.
52 D. S. Charles, M. Feygenson, K. Page, J. Neuefeind, W. Xu and X. Teng, *Nat. Commun.*, 2017, **8**, 1–8.
53 Q. T. Qu, L. L. Liu, Y. P. Wu and R. Holze, *Electrochim. Acta*, 2013, **96**, 8–12.
54 G. Liang, Z. Gan, X. Wang, X. Jin, B. Xiong, X. Zhang, S. Chen, Y. Wang, H. He and C. Zhi, *ACS Nano*, 2021, **15**, 17717–17728.
55 G. Liang, X. Li, Y. Wang, S. Yang, Z. Huang, Q. Yang, D. Wang, B. Dong, M. Zhu and C. Zhi, *Nano Res. Energy*, 2022, **1**, e9120002.
56 A. Zhou, W. Cheng, W. Wang, Q. Zhao, J. Xie, W. Zhang, H. Gao, L. Xue and J. Li, *Adv. Energy Mater.*, 2021, **11**, 2000943.
57 R. Y. Wang, B. Shyam, K. H. Stone, J. N. Weker, M. Pasta, H. W. Lee, M. F. Toney and Y. Cui, *Adv. Energy Mater.*, 2015, **5**, 1401869.
58 H. J. Buser, D. Schwarzenbach, W. Petter and A. Ludi, *Inorg. Chem.*, 1977, **16**, 2704–2710.
59 F. Herren, P. Fischer, A. Ludi and W. Haelg, *Inorg. Chem.*, 1980, **19**, 956–959.
60 K. Itaya, I. Uchida and V. D. Neff, *Acc. Chem. Res.*, 1986, **19**, 162–168.
61 K. Hurlbutt, S. Wheeler, I. Capone and M. Pasta, *Joule*, 2018, **2**, 1950–1960.
62 C. D. Wessells, S. V. Peddada, M. T. McDowell, R. A. Huggins and Y. Cui, *J. Electrochem. Soc.*, 2011, **159**, A98.
63 D. Yang, J. Xu, X.-Z. Liao, Y.-S. He, H. Liu and Z.-F. Ma, *Chem. Commun.*, 2014, **50**, 13377–13380.
64 Y. Moritomo, S. Urase and T. Shibata, *Electrochim. Acta*, 2016, **210**, 963–969.
65 G. Li, B. Huang, Z. Pan, X. Su, Z. Shao and L. An, *Energy Environ. Sci.*, 2019, **12**, 2030–2053.
66 Y. Zhong, X. Xu, J.-P. Veder and Z. Shao, *iScience*, 2020, **23**, 100943.
67 C. Masquelier and L. Croguennec, *Chem. Rev.*, 2013, **113**, 6552–6591.
68 X. Zhang, X. Rui, D. Chen, H. Tan, D. Yang, S. Huang and Y. Yu, *Nanoscale*, 2019, **11**, 2556–2576.
69 Q. Wang, J. Xu, W. Zhang, M. Mao, Z. Wei, L. Wang, C. Cui, Y. Zhu and J. Ma, *J. Mater. Chem. A*, 2018, **6**, 8815–8838.
70 G. Chen, Q. Huang, T. Wu and L. Lu, *Adv. Funct. Mater.*, 2020, **30**, 2001289.
71 X. Xu, F. Xiong, J. Meng, X. Wang, C. Niu, Q. An and L. Mai, *Adv. Funct. Mater.*, 2020, **30**, 1904398.
72 Y.-L. Ding, Y. Wen, C. Wu, P. A. van Aken, J. Maier and Y. Yu, *Nano Lett.*, 2015, **15**, 1388–1394.
73 X. Xu, F. Xiong, J. Meng, Q. An and L. Mai, *Mater. Today Nano*, 2020, **10**, 100073.
74 H. Tang, Z. Peng, L. Wu, F. Xiong, C. Pei, Q. An and L. Mai, *Electrochem. Energy Rev.*, 2018, **1**, 169–199.
75 S. Zhang, H. Tan, X. Rui and Y. Yu, *Acc. Chem. Res.*, 2020, **53**, 1660–1671.
76 Y. Zhang, E. H. Ang, K. N. Dinh, K. Rui, H. Lin, J. Zhu and Q. Yan, *Mater. Chem. Front.*, 2021, **5**, 744–762.
77 X. Li, Z. Huang, C. E. Shuck, G. Liang, Y. Gogotsi and C. Zhi, *Nat. Rev. Chem.*, 2022, **6**, 389–404.
78 F. Ming, H. Liang, G. Huang, Z. Bayhan and H. N. Alshareef, *Adv. Mater.*, 2021, **33**, 2004039.
79 X. Li, X. Ma, Y. Hou, Z. Zhang, Y. Lu, Z. Huang, G. Liang, M. Li, Q. Yang, J. Ma, N. Li, B. Dong, Q. Huang, F. Chen, J. Fan and C. Zhi, *Joule*, 2021, **5**, 2993–3005.
80 Y. Tian, Y. An, J. Feng and Y. Qian, *Mater. Today*, 2022, **52**, 225–249.
81 R. Zhao, A. Elzatahry, D. Chao and D. Zhao, *Matter*, 2022, **5**, 8–10.
82 X. Li, Q. Li, Y. Hou, Q. Yang, Z. Chen, Z. Huang, G. Liang, Y. Zhao, L. Ma, M. Li, Q. Huang and C. Zhi, *ACS Nano*, 2021, **15**, 14631–14642.
83 Y. Li, W. Deng, Z. Zhou, C. Li, M. Zhang, X. Yuan, J. Hu, H. Chen and R. Li, *J. Mater. Chem. A*, 2021, **9**, 2822–2829.
84 D. P. Leonard, Z. Wei, G. Chen, F. Du and X. Ji, *ACS Energy Lett.*, 2018, **3**, 373–374.
85 T. Liu, L. Tang, H. Luo, S. Cheng and M. Liu, *Chem. Commun.*, 2019, **55**, 12817–12820.
86 X. Yuan, Y. Li, Y. Zhu, W. Deng, C. Li, Z. Zhou, J. Hu, M. Zhang, H. Chen and R. Li, *ACS Appl. Mater. Interfaces*, 2021, **13**, 38248–38255.
87 Y. Mao, M. Xie, W. Zhao, K. Yuan, Y. Fang and F. Huang, *RSC Adv.*, 2019, **9**, 32323–32327.
88 M. Xie, W. Zhao, Y. Mao and F. Huang, *Dalton Trans.*, 2020, **49**, 3488–3494.
89 N. D. Schuppert, S. Mukherjee, A. M. Bates, E.-J. Son, M. J. Choi and S. Park, *J. Power Sources*, 2016, **316**, 160–169.
90 Y.-Q. Li, H. Shi, S.-B. Wang, Y.-T. Zhou, Z. Wen, X.-Y. Lang and Q. Jiang, *Nat. Commun.*, 2019, **10**, 1–9.
91 A. Schmidt, M. K. Ramos, C. M. Ferreira, B. A. Braz and A. J. G. Zarbin, *Electrochim. Acta*, 2021, **387**, 138500.
92 T. Qin, X. Chu, T. Deng, B. Wang, X. Zhang, T. Dong, Z. Li, X. Fan, X. Ge and Z. Wang, *J. Energy Chem.*, 2020, **48**, 21–28.
93 T. Qin, W. Zhang, Y. Ma, W. Zhang, T. Dong, X. Chu, T. Li, Z. Wang, N. Yue and H. Liu, *Energy Storage Mater.*, 2022, **45**, 33–39.
94 H. Chen, Z. Zhang, Z. Wei, G. Chen, X. Yang, C. Wang and F. Du, *Sustainable Energy Fuels*, 2020, **4**, 128–131.
95 M. Wang, H. Wang, H. Zhang and X. Li, *J. Energy Chem.*, 2020, **48**, 14–20.
96 Y. Liang, Y. Jing, S. Gheytani, K.-Y. Lee, P. Liu, A. Facchetti and Y. Yao, *Nat. Mater.*, 2017, **16**, 841–848.
97 J. Han, Y. Niu, S.-J. Bao, Y.-N. Yu, S.-Y. Lu and M. Xu, *Chem. Commun.*, 2016, **52**, 11661–11664.
98 Z. Wei, D. Wang, M. Li, Y. Gao, C. Wang, G. Chen and F. Du, *Adv. Energy Mater.*, 2018, **8**, 1801102.
99 J. Mei, T. Liao, L. Kou and Z. Sun, *Adv. Mater.*, 2017, **29**, 1700176.
100 H. Tan, Y. Feng, X. Rui, Y. Yu and S. Huang, *Small Methods*, 2020, **4**, 1900563.
101 X. Liu, J.-Q. Huang, Q. Zhang and L. Mai, *Adv. Mater.*, 2017, **29**, 1601759.
102 Q. Pan, Z. Tong, Y. Su, S. Qin and Y. Tang, *Adv. Funct. Mater.*, 2021, **31**, 2103912.

103 Y. Jiang, Y. Wang, J. Ni and L. Li, *InfoMat*, 2021, **3**, 339–352.
104 S. H. Lee, Y. H. Kim, R. Deshpande, P. A. Parilla, E. Whitney, D. T. Gillaspie, K. M. Jones, A. H. Mahan, S. Zhang and A. C. Dillon, *Adv. Mater.*, 2008, **20**, 3627–3632.
105 M. Zheng, H. Tang, Q. Hu, S. Zheng, L. Li, J. Xu and H. Pang, *Adv. Funct. Mater.*, 2018, **28**, 1707500.
106 K. Song, C. Liu, L. Mi, S. Chou, W. Chen and C. Shen, *Small*, 2021, **17**, 1903194.
107 X. Wang, S. Tang, W. Guo, Y. Fu and A. Manthiram, *Mater. Today*, 2021, **50**, 259–275.
108 J. Wang, Z. Liu, J. Zhou, K. Han and B. Lu, *ACS Mater. Lett.*, 2021, **3**, 1572–1598.
109 H. Wang, D. Yu, X. Wang, Z. Niu, M. Chen, L. Cheng, W. Zhou and L. Guo, *Angew. Chem., Int. Ed.*, 2019, **58**, 16451–16455.
110 S. Ji, C. Song, J. Li, K. S. Hui, W. Deng, S. Wang, H. Li, D. A. Dinh, X. Fan, S. Wu, J. Zhang, F. Chen, Z. Shao and K. N. Hui, *Adv. Energy Mater.*, 2021, **11**, 2101413.
111 Y. Chen, W. Luo, M. Carter, L. Zhou, J. Dai, K. Fu, S. Lacey, T. Li, J. Wan, X. Han, Y. Bao and L. Hu, *Nano Energy*, 2015, **18**, 205–211.
112 S. Xu, Y. Chen and C. Wang, *J. Mater. Chem. A*, 2020, **8**, 15547–15574.
113 C. Han, J. Zhu, C. Zhi and H. Li, *J. Mater. Chem. A*, 2020, **8**, 15479–15512.
114 Y. Liang, C. Luo, F. Wang, S. Hou, S.-C. Liou, T. Qing, Q. Li, J. Zheng, C. Cui and C. Wang, *Adv. Energy Mater.*, 2019, **9**, 1802986.
115 A. V. Desai, R. E. Morris and A. R. Armstrong, *ChemSusChem*, 2020, **13**, 4866–4884.
116 H. Cui, L. Ma, Z. Huang, Z. Chen and C. Zhi, *SmartMat*, 2022, DOI: **10.1002/smm2.1110**.
117 X. Zhang, J. Meng, X. Wang, Z. Xiao, P. Wu and L. Mai, *Energy Storage Mater.*, 2021, **38**, 30–49.
118 S. Chen, M. Zhang, P. Zou, B. Sun and S. Tao, *Energy Environ. Sci.*, 2022, **15**, 1805–1839.
119 J. Huang, Z. Guo, Y. Ma, D. Bin, Y. Wang and Y. Xia, *Small Methods*, 2019, **3**, 1800272.
120 H. Ao, Y. Zhao, J. Zhou, W. Cai, X. Zhang, Y. Zhu and Y. Qian, *J. Mater. Chem. A*, 2019, **7**, 18708–18734.
121 J. Yan, J. Wang, H. Liu, Z. Bakenov, D. Gosselink and P. Chen, *J. Power Sources*, 2012, **216**, 222–226.
122 J. Zhang, Z. Cao, L. Zhou, G. Liu, G.-T. Park, L. Cavallo, L. Wang, H. N. Alshareef, Y.-K. Sun and J. Ming, *ACS Energy Lett.*, 2020, **5**, 2651–2661.
123 Y. Lv, Y. Xiao, L. Ma, C. Zhi and S. Chen, *Adv. Mater.*, 2022, **34**, 2106409.
124 Y. Wang, J. Yi and Y. Xia, *Adv. Energy Mater.*, 2012, **2**, 830–840.
125 R. B. McCleskey, *J. Chem. Eng. Data*, 2011, **56**, 317–327.
126 R. J. Gilliam, J. W. Graydon, D. W. Kirk and S. J. Thorpe, *Int. J. Hydrogen Energy*, 2007, **32**, 359–364.
127 L. Suo, O. Borodin, T. Gao, M. Olguin, J. Ho, X. Fan, C. Luo, C. Wang and K. Xu, *Science*, 2015, **350**, 938–943.
128 M. R. Lukatskaya, J. I. Feldblyum, D. G. Mackanic, F. Lissel, D. L. Michels, Y. Cui and Z. Bao, *Energy Environ. Sci.*, 2018, **11**, 2876–2883.
129 Y. Zhu, J. Yin, X. Zheng, A.-H. Emwas, Y. Lei, O. F. Mohammed, Y. Cui and H. N. Alshareef, *Energy Environ. Sci.*, 2021, **14**, 4463–4473.
130 H. Gao, K. Tang, J. Xiao, X. Guo, W. Chen, H. Liu and G. Wang, *J. Energy Chem.*, 2022, **69**, 84–99.
131 S. Ko, Y. Yamada and A. Yamada, *Electrochem. Commun.*, 2020, **116**, 106764.
132 Q. Zheng, S. Miura, K. Miyazaki, S. Ko, E. Watanabe, M. Okoshi, C. P. Chou, Y. Nishimura, H. Nakai and T. Kamiya, *Angew. Chem., Int. Ed.*, 2019, **131**, 14340–14345.
133 S. S. Zhang, *J. Power Sources*, 2006, **162**, 1379–1394.
134 S. Guo, L. Qin, T. Zhang, M. Zhou, J. Zhou, G. Fang and S. Liang, *Energy Storage Mater.*, 2021, **34**, 545–562.
135 G. G. Eshetu, M. Martinez-Ibañez, E. Sánchez-Diez, I. Gracia, C. Li, L. M. Rodriguez-Martinez, T. Rojo, H. Zhang and M. Armand, *Chem. – Asian J.*, 2018, **13**, 2770–2780.
136 F. Wang, Y. Lin, L. Suo, X. Fan, T. Gao, C. Yang, F. Han, Y. Qi, K. Xu and C. Wang, *Energy Environ. Sci.*, 2016, **9**, 3666–3673.
137 Y. Du, Y. Li, B. B. Xu, T. X. Liu, X. Liu, F. Ma, X. Gu and C. Lai, *Small*, 2021, 2104640.
138 A. M. Haregewoin, A. S. Wotango and B.-J. Hwang, *Energy Environ. Sci.*, 2016, **9**, 1955–1988.
139 H. Zhang, G. G. Eshetu, X. Judez, C. Li, L. M. Rodriguez-Martínez and M. Armand, *Angew. Chem., Int. Ed.*, 2018, **57**, 15002–15027.
140 L. Li, S. Zhao, Z. Hu, S.-L. Chou and J. Chen, *Chem. Sci.*, 2021, **12**, 2345–2356.
141 J. Cao, D. Zhang, X. Zhang, Z. Zeng, J. Qin and Y. Huang, *Energy Environ. Sci.*, 2022, **15**, 499–528.
142 F. Wan, L. Zhang, X. Dai, X. Wang, Z. Niu and J. Chen, *Nat. Commun.*, 2018, **9**, 1656.
143 N. Li, G. Li, C. Li, H. Yang, G. Qin, X. Sun, F. Li and H.-M. Cheng, *ACS Appl. Mater. Interfaces*, 2020, **12**, 13790–13796.
144 W. Xu, K. Zhao, W. Huo, Y. Wang, G. Yao, X. Gu, H. Cheng, L. Mai, C. Hu and X. Wang, *Nano Energy*, 2019, **62**, 275–281.
145 S. J. Banik and R. Akolkar, *Electrochim. Acta*, 2015, **179**, 475–481.
146 K. E. K. Sun, T. K. A. Hoang, T. N. L. Doan, Y. Yu and P. Chen, *Chem. – Eur. J.*, 2018, **24**, 1667–1673.
147 T. Otani, Y. Fukunaka and T. Homma, *Electrochim. Acta*, 2017, **242**, 364–372.
148 Z. Wang, H. Li, Z. Tang, Z. Liu, Z. Ruan, L. Ma, Q. Yang, D. Wang and C. Zhi, *Adv. Funct. Mater.*, 2018, **28**, 1804560.
149 S. Huang, F. Wan, S. Bi, J. Zhu, Z. Niu and J. Chen, *Angew. Chem., Int. Ed.*, 2019, **131**, 4357–4361.
150 Y. Xia, N. Xu, L. Du, Y. Cheng, S. Lei, S. Li, X. Liao, W. Shi, L. Xu and L. Mai, *ACS Appl. Mater. Interfaces*, 2020, **12**, 22930–22938.
151 Y. Cheng, J. Shu, L. Xu, Y. Xia, L. Du, G. Zhang and L. Mai, *Adv. Energy Mater.*, 2021, **11**, 2100026.
152 H. Yin, C. Han, Q. Liu, F. Wu, F. Zhang and Y. Tang, *Small*, 2021, **17**, 2006627.

